

Recurrent Quantification Analysis of Movement Variability in Human-Humanoid Interaction Activities

Miguel Xochicale^{1,*} and Chris Baber¹

¹University of Birmingham, School of Engineering, Birmingham, B15 2TT, UK
*map479@bham.ac.uk

ABSTRACT

Human movement variability occurs in motor performance across multiple repetitions of a task and such behaviour is an inherent feature within and between each persons' movement. Quantifying movement variability is still an open problem, particularly when methods in time domain, frequency domain or nonlinear dynamics can break down due to the real-world time-series datasets. For this work, we therefore investigate nonlinear dynamics methods such as reconstructed state space (RSSs), uniform time-delay embedding, recurrence plots (RPs) and recurrence quantification analysis metrics (RQAs) with real-world time-series data. Particularly, we are interested in the weaknesses and robustness of nonlinear dynamics tools with the use of raw and post-processed data of wearable inertial sensors. That said, twenty right-handed healthy participants imitated simple vertical and horizontal arm movements in normal and faster velocity from an humanoid robot in order to have four window lengths and three levels of smoothed time-series data, to then found visual differences in the patterns with RSSs and RPs and particularly the computed differences with RQA metrics that help us to quantify activities, types of sensors, windows lengths and level of smoothness. Specifically, we can conclude that RQA ENTR, Shannon Entropy, can lead to interesting results on the quantification of movement variability for participants of different ages, state of health and anthropomorphic features to then enhance the development of better diagnostic tools for applications in rehabilitation, sport science or for new forms of human-humanoid interaction.

Introduction

Human movement requires a complex system where not only multiple joints and limbs are involved for a specific task in a determined environment but also perception and action of movement that affects such physical performance¹. In contrast, variability in humanoid movement is usually very small, as a result of mechanical and dynamic capabilities². This means that, while humanoids solve the degrees of freedom problem through joint design and algorithms, humans tend to have more fluid and flexible approach. Consequently, one can see much variability in human movement performance of even the simplest task. Studies of human motion reveal the possibility to estimate features from lower dimension signals to distinguish differences between styles of pedalling motion^{3,4}, gait identification^{5,6}, and detection of pathologies⁷. The lower dimension signals from biological systems are time series of 1–dimension in \mathbb{R} which commonly are noisy, nonlinear and non-stationary⁷. Hence, nonlinear dynamics can be used to objectively quantify variability of lower dimension signals^{3–9}. For instance, Bradley et al. 2015¹⁰ reviewed methods for nonlinear time series analysis based on the estimation of the embedding parameters (m embedding dimension and τ embedding delay) to reconstruct the state space, where an n -dimensional reconstructed state space using 1–dimensional time series, can preserve the topological properties of an unknown M -dimensional state space¹¹. Similarly, Bradley et al. 2015¹⁰ reviewed the use of Recurrence Plots (RPs), a graphical representation of a two-dimensional map which show black and white dots as recurrences in a given n -dimensional system, and Recurrence Quantification Analysis (RQA) metrics that compute statistics in RPs. In general, RPs and RQA provide an intuitive meaning of the time series, for instance, RQA is quantitatively and qualitatively independent of embedding dimension (also verified experimentally¹²). However, the estimation of embedding parameters and the selection of the right parameters to perform RQA is still an open problem. Bradley et al. 2015¹⁰ pointed out that there is no general technique that can be used to compute the embedding parameters since time series are system-dependent which means that computing the values for embedding parameters may only work for one purpose (e.g., prediction) and may not work well for another purpose (e.g., computing dynamical invariants). Additionally, methods of nonlinear dynamics for computing embedding parameters e.g., autocorrelation, mutual information, and nearest neighbour require data which is well sampled and with little noise¹³ or require signals that are purely deterministic¹⁴. Thus, these methods of nonlinear analysis for computing the embedding parameters can break down with real-world datasets which have generally different length, different values of accuracy and precision (rounding errors due to finite precision of the measurement apparatus which include frequency acquisition⁶), and contaminated data with different sources of noise¹³. It is then surprising that even with the previous constraints with regard to the quality of data, and the problem with the estimation of embedding parameters,

the use of nonlinear dynamics have proven to be helpful to understand and to characterise dynamics of time series^{3–7, 7–10}.

For this work, we are interested in exploring and investigating the effects of different features of time series (e.g. levels of smoothness, window data length, structures of time series based on types of movements, types of sensors, participants and velocities) to estimate embedded parameters for uniform time-delay embedding, recurrence plots and recurrence quantification analysis. Hence, we conducted an experiment with twenty right-handed healthy participants in the context of human-humanoid imitation activities where participants were asked to imitate simple arm movements performed by a humanoid robot. The primary aim of this work is to explore the following questions:

- What are the effects on three nonlinear methods (reconstructed state space with uniform time-delay embedding, Recurrence Plots, and Recurrence Quantification Analysis), for different embedding parameters, different recurrence thresholds and different characteristics of time series (structure of the signal, window length and smoothness of the signal)?, and
- What are the strengths and weaknesses of Recurrence Quantification Analysis for the previous conditions of nonlinear analysis methods?

Results

Reconstructed State Spaces

One of the challenges of the implementation of uniform time-delay embedding to reconstruct the state spaces is the selection of embedding parameters because each time series is unique in terms of its structure (e.g. modulation of amplitude, frequency and phase)^{5, 6, 10}. With that in mind, the problem for this work is not to compute individual embedding parameters for each of the time series but to deal with a selection of two parameters that can represent all the time series. Our solution for such problem, as explained in below sections, was to compute a sample mean over all values in each of the conditions of the time series for minimum dimension values and for minimum delay values.

Minimum embedding parameters

Minimum embedding parameters were firstly computed with the methods of False Nearest Neighbour and Average Mutual Information. Figures 1(A) show box plots for the minimum embedding values for sensors HS01 and RS01. Minimum embedding values for HS01 presents more variations than RS01 as interquartile range for HS01 is near to 1 (with the exceptions of HF sg0, VN sg0, and VF sg1) whereas interquartile range for RS01 is near to 0.1 (with the exception of two axis HF sg0 and VF sg1). Additionally, Figures 1(A) show a decrease of mean values (rhombus) in the box plots as smoothness of time series increase (see sg0, sg1, sg2). Figures 1(B) show box plots for the first minimum values of AMI values. It can be seen that values for HS01 tend to be more spread as the smoothness of the time series is increasing (see the increase of both mean (rhombus) and interquartile range). However, AMI values for RS01 do not show such increase in relation with the increase of smoothness except for HF and VF (Figs 1(B)).

We also computed a sample mean for an overall minimum embedding parameters that represent all participants, activities, sensors and levels of smoothness. The sample mean for the minimum values of $E_1(m)$ from Figs 1(A) is $\bar{m}_0 = 6$ and the sample mean for minimum values of AMIs from Figs 1(B) is $\bar{\tau}_0 = 8$.

Uniform Time-Delay Embedding

Uniform time-delay embedding were computed with the overall embedding parameters ($\bar{m}_0 = 6$, $\bar{\tau}_0 = 8$) and the first three axis of the rotated data of the PCA are shown for the reconstructed state spaces of horizontal arm movements (Figs 2) and vertical arm movements (Figs 3).

One can observe by eye the differences in each of the trajectories of the reconstructed state spaces (Figs 2 and 3), however an objective quantification is required. That being said, we tried to quantify those differences using euclidean distances between the origin to each of the points in their trajectories, which results did not capture the dynamics of the trajectories specially for those that looked very messy. Such ambiguities lead us to consider the use of Recurrence Plots and Recurrence Quantification Analysis to objectively quantify dynamics the capture activities using time series.

Recurrences Plots

Recurrence Plots (RP) were computed for horizontal arm movements (Fig 4) and vertical arm movements (Fig 5) using the average embedding parameters ($\bar{m}_0 = 6$, $\bar{\tau}_0 = 8$) and an recurrence threshold of $\varepsilon = 1$.

Recurrence Quantification Analysis

Four Recurrence Quantification Analysis (RQA) metrics (REC, DET, RATIO and ENTR) were also computed with $\bar{m}_0 = 6$, $\bar{\tau}_0 = 8$, and $\varepsilon = 1$.

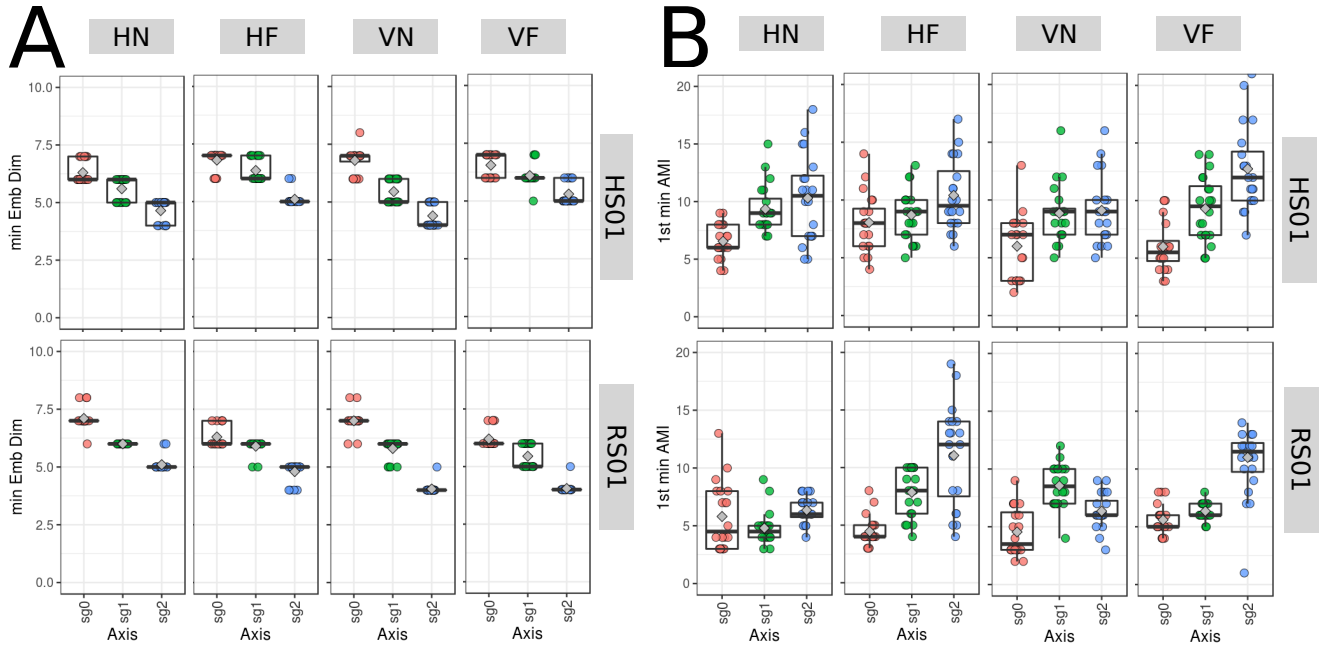


Figure 1. Box plots of minimum embedding parameters. Box plots of (A) minimum embedding dimensions and (B) first minimum AMI values for Horizontal Normal (HN), Horizontal Faster (HF), Vertical Normal (VN) and Vertical Faster (VF) with sensors attached to participants (HS01) and sensor attached to robot (RS01). Minimum embedding parameters are for twenty participants (p_01 to p_{20}) with three smoothed signals (sg0: sg0zmuvGyroZ, sg1: sg1zmuvGyroZ and sg2: sg2zmuvGyroZ) and window length of 10-sec (500 samples). Code and data to reproduce the figure is available in ¹⁵.

REC values

Figs 6(A) show box plots of REC values that represent the % of black dots in RPs. It can be noted that REC values are more spread for HN and VN movements (higher interquartile range) than for HF and VF movements (lower interquartile range) for HS01 sensor. In contrast, REC values for RS01 sensor present little variation (interquartile range of 0.01). Regarding the increase of smoothness for time series (sg0, sg1 and sg2), REC values present little variation as the smoothness is increasing for time series from HS01 (changes of mean values (rhombus)) whereas REC values are more affected with the smoothness for data from RS01 (see the incremental changes of mean values (rhombus)).

DET values

Figs 6(B) illustrate DET values that represent the predictability and organisation of RPs. Generally, it can be noted little change of DET values (interquartile range is around 0.1) for type of movement, type of sensor but the increase of DET values as the smoothness of the signal increase (see the incremental changes of mean values (rhombus)). However, the interquartile range for faster movements (HF and VF) with no smoothing (sg0) is lower than the other levels of smoothness (sg1 and sg2).

RATIO values

Figs 6(C) illustrate RATIO values that represent the dynamic transitions in RPs. Generally, it can be seen that RATIO values for HS01 sensor vary less for HN movements (interquartile range around 2) than HF movements (interquartile range around 5). For faster movements (HF and VF), it can be noted a decrease of the mean values the smoothness of the time series is increasing (rhombus). However, for normal movements (HN and VN), the decrease of mean values is less evident than faster movements (rhombus).

ENTR values

Figs 6(D) show ENTR values that represent Shannon entropy values in RPs. Generally, ENTR values for HS01 sensor show a higher variation (interquartile range around 0.5) than ENTR values for RS01 sensor (interquartile range 0.1). It can also be noted the increase of mean values for ENTR values as the smoothness of time series increase (rhombus) for type of movement, type of sensor and level of smoothness.

3D RQA ENTR

To show how that the selection of recurrence threshold affects RQA values, we computed ENTR values of RQA metrics for different embedding parameters $\{m \in \mathbb{R} | 1 \leq m \leq 10\}$, $\{\tau \in \mathbb{R} | 1 \leq \tau \leq 10\}$ incrementing by one, with the consideration of three recurrence thresholds $\varepsilon = 1, 2, 3$ and three levels of smoothness (sg0, sg1, sg2). For instance, Figures 7 show the increase of recurrence threshold is associated to the increase of ENTR values in any of the levels of smoothness (see values of the ENTR bar). Similarly, it can be noted that the increase of level of smoothness (sg0, sg1 and sg2) is associated with the increase of ENTR values of the 3D surface plots. Figures 8 show 3D surface plots of ENTR values for different sensors and different activities. Figs 8 show that RQA ENTR (lateral bars) decrease from normal (HN, VN) to faster (HF, VF) velocities from both human sensor (HS01) to robot sensor (RS01). Also, it can be noted that RQA ENTR values decrease from human sensor (HS01) to robot sensor (RS01). Figures 9 show the similarity of 3D surface plots in relationship with three participants (p01, p02 and p03) performing four activities (HN, HF, VN, and VF) and two sensors (HS01, RS01). Figures 9(A) present subtle differences for each of the participants (see RQA ENTR bar). Figures 9(B) show less change of RQA ENTR values for each participant as the data is from a sensor attached to the robot. Also, from data of sensors attached to the robot, it can be noted that changes are more notable for faster movements than normal movements. Figures 10 show the effect of the increase of window length of the time series (w100 (2-sec), w250 (5-sec), w500 (10-sec) and w750 (15-sec)) on the 3D surface plots. It can be noted that the increase of number of samples improves the quality of the surface plots where 100 samples poorly capture the dynamics of each activity. However as the window length increases from 250, 500 to 750 samples, 3D surface plots show a similar representation of RQA ENTR values (being the surface plot with 750 samples the best test case).

To summarise this section of results, it can be said that computing embedding parameters for individual structure of time-series data is already a solved problem^{5,6,10}. However, it has been shown the challenge of finding embedding parameters for nonlinear dynamic tools that represent a set of different time-series data. That said, we proposed the use of sample mean of the set of embedding parameters for RSSs, RP and RQA to then noticed that the selection of recurrence threshold, ε , is also an open problem. For which, this work proposed the variation of recurrence thresholds and embedding parameters to show the relationships of these to different datasets (participants, activities, windows lengths and sensors).

Discussion

Time series from different sources (e.g., participants, movements, axis type) as well as different characteristics (e.g., sample rate, window length or levels of smoothness) result in different embedding parameters and therefore different values for recurrence plots and recurrence quantification analysis metrics. That said, while embedding parameters for individual time series were successfully computed, the quantification of variability with regard to the shape of the trajectories in reconstructed state spaces require more investigation as our initial, approach based on euclidean distances on the trajectories, failed to quantify trajectories which were not well unfolded. To then found out that Recurrence Plots along with Recurrence Quantification Analysis (RQA) metrics (e.g., REC, DET, RATIO and ENTR) and its variation of embedding parameters and recurrence thresholds helped to quantify the variability of different sources of time series. However, further investigation is required to be done in order to have better intuition and meaningful interpretation of nonlinear analysis such as to find a right balance among (i) the level of smoothness of the signal, (ii) the selection of recurrence thresholds and (iii) the range of embedding parameters.

Conclusions

This work allows to conclude that the choice of nonlinear analysis tool (e.g., RSSs, RPs, RQA metrics) will depend on what one would like to quantify on the time-series data (e.g., predictability, organisation, dynamics transitions, or complexity and determinism). Then, time-series data characteristics (e.g., window size length, level of smoothness) plays an important role as well on the results that nonlinear analysis tool can provide. Similarly, the results of the nonlinear analysis tools are associated with the structure of the time-series data (e.g. frequency, amplitude), the position of the sensor and activity performed by either a robot or human being (as degrees of freedom from the humanoid are far less than human movement). That said, it has been shown that the use of different characteristics of the time-series data (e.g., sensor, activity, level of smoothness and participants) has help us to visualise and to quantify with nonlinear tools the variation of movements of, in this work, human-humanoid activities. However, some limitation of nonlinear tools are related to the computation of different parameters (e.g., recurrence thresholds, embedding parameters) that reflect the dynamics of individual characteristics of activity type, window length and structure of the time series. Specifically, the example of DET values which appear to be constants across sensors, activities and levels of smoothness, whereas REC and RATIO, as function of REC, values show variation for certain sensors and movements. To then found out that RQA ENTR values with different recurrence thresholds were appropriate to quantify the different changes and variations of the characteristics of time-series data. Therefore, we can conclude that this work provides a good starting point and reference to the use of Shannon Entropy to quantify human-humanoid imitation activities that can then

lead to interesting results on the quantification of movement variability of participants with different ages, state of health and anthropomorphic features.

Methods

State Space Reconstruction

The method of state space reconstruction¹⁶¹¹ has been applied in many disciplines^{4–6,9,17}. The method of state space reconstruction is based on uniform time-delay embedding methodology which is a simple matrix implementation that can reconstruct an unknown d -dimensional manifold M from a scalar time series (e.g. one-dimensional time series in \mathbb{R}). A manifold, in this context, is a multidimensional curved surface within a space (e.g. a saddle)¹⁸.

The use of a scalar time series is the main advantage of the method of state space reconstruction which in essence preserve dynamic invariants such as correlation dimension, fractal dimension, Lyapunov exponents, Kolmogorov-Sinai entropy and detrended fluctuation analysis^{3,4,10,19,20}. However, selecting appropriate embedding parameters which are used to apply the state space reconstruction is still an open challenge for which we present introductions for the methodologies to compute such embedding parameters. With that in mind, in the following subsections, we describe in more detail the state space reconstruction theorem (RSSs), uniform time-delay embedding theorem (UTDE), false nearest neighbours (FNN) and average mutual information (AMI).

State Space Reconstruction Theorem

Following the notation employed in^{11,13,21–24}, state space reconstruction is defined by:

$$s(t) = f^t[s(0)], \quad (1)$$

where $s, s : A \rightarrow M$ given that $A \subseteq \mathbb{R}$ and $M \subseteq \mathbb{R}^d$, represents a trajectory which evolves in an unknown d -dimensional manifold M , $f : M \rightarrow M$ is an evolution function and f^t , with time evolution $t \in \mathbb{N}$, is the t -th iteration of f that corresponds to an initial position $s(0) \in M^{11}$. Then, a point of a one-dimensional time series $x(t)$ in \mathbb{R} , can be obtained with

$$x(t) = h[s(t)], \quad (2)$$

where h is a function, $h : M \rightarrow \mathbb{R}$, defined on the trajectory $s(t)$. Reconstructed state space can then be described as an n -dimensional state space defined by $y(t) = \Psi[X(t)]$ where $X(t) = \{x(t), x(t - \tau), \dots, x(t - (m - 1)\tau)\}$ is the uniform time-delay embedding with a dimension embedding m and delay embedding τ and $\Psi : \mathbb{R}^m \rightarrow \mathbb{R}^n$ is a further transformation of dimensionality (e.g. Principal Component Analysis, Singular Value Decomposition, etc) being $n \leq m$. With that in mind, uniform time-delay embedding, $X(t)$, defines a map $\Phi : M \rightarrow \mathbb{R}^m$ such that $X(t) = \Phi(s(t))$, where Φ is a diffeomorphic map¹¹ whenever $\tau > 0$ and $m > 2d_{box}$ and d_{box} is the box-counting dimension of M^{13} . Then, if Φ is an embedding of evolving trajectories in the reconstructed space then a composition of functions represented with F^t is induced on the reconstructed state space determined:

$$X(t) = F^t[X(0)] = \Phi \circ f^t \circ \Phi^{-1}[X(0)]. \quad (3)$$

With this in mind, an embedding is defined as "a smooth one-to-one coordinate transformation with a smooth inverse" and the total reconstruction map is defined as $\Xi = \Psi \circ \Phi^{21}$. Fig 11 illustrates the state space reconstruction.

Uniform Time-Delay Embedding (UTDE)

Frank et al. and Sama et al. refer to the state space reconstruction as "time-delay embeddings" or "delay coordinates"^{5,6}. However, we consider the term "uniform time-delay embedding" as more descriptive and appropriate terminology for our work. Hence, the uniform time-delay embedding is represented as a matrix of uniform delayed copies of the time series $\{x_n\}_{n=1}^N$ where N is the sample length of $\{x_n\}$ and n is index for the samples of $\{x_n\}$. $\{x_n\}_{n=1}^N$ has a sample rate of T . The delayed copies of $\{x_n\}$ are uniformly separated by τ and represented as $\{\tilde{x}_{n-i\tau}\}$ where i goes from $0, 1, \dots, (m - 1)$. Generally speaking, $\{\tilde{x}_{n-i\tau}\}$ contains information of unobserved state variables and encapsulates the information of the delayed copies of the available time series in the uniform time-delay embedding matrix X_τ^m , $X_\tau^m \in \mathbb{R}^m$, defined as

$$X_\tau^m = \begin{pmatrix} \tilde{x}_n \\ \tilde{x}_{n-\tau} \\ \tilde{x}_{n-2\tau} \\ \vdots \\ \tilde{x}_{n-(m-1)\tau} \end{pmatrix}^\top, \quad (4)$$

where m is the embedding dimension, τ is the embedding delay and $^\top$ denotes the transpose. m and τ are known as embedding parameters. The matrix dimension of X_τ^m is defined by $N - (m - 1)\tau$ rows and m columns and $N - (m - 1)\tau$ defines the length of each delayed copy of $\{\tilde{x}_n\}$ in X_τ^m .

Estimation of Embedding Parameters

The estimation of the embedding parameters (m and τ) is a fundamental step for the state space reconstruction with the use of uniform time-delay embedding method. With this in mind, we review two of the most common algorithms, which will be used in our work, to compute the embedding parameters: the false nearest neighbour (FNN) and the average mutual information (AMI).

False Nearest Neighbours

To select the minimum embedding dimension m_0 , Kennel et al.²⁵ used the method of false neighbours which can be understood as follows: on the one hand, when the embedding dimension is too small to unfold the attractor "not all points that lie close each other will be neighbours and some points appear as neighbours because of the attractor has been projected down into an smaller space", on the other hand, when increasing the embedding dimension "points that are near to each other in the sufficient embedding dimension should remain close as the dimension increase from m to $m + 1$ ²⁰". From a mathematical point of view, the state space reconstruction theorem is done when the attractor is unfolded with either the minimum embedding dimension, m_0 , or any other embedding dimension value where $m \geq m_0$ ²⁵. On the contrary, any large value of m_0 leads to excessive computations¹⁰. With this in mind, Cao²⁶ proposed an algorithm based on the false neighbour method where only the time-series and one delay embedding value are necessary to select the minimum embedding dimension. Cao's algorithm is based on $E(m)$ which is the mean value of all $a(i, m)$, both defined as follows

$$\begin{aligned} E(m) &= \frac{1}{N-m\tau} \sum_{i=1}^{N-m\tau} a(i, m) \\ &= \frac{1}{N-m\tau} \sum_{i=1}^{N-m\tau} \frac{\|X_i(m+1) - X_{n(i,m)}(m+1)\|}{\|X_i(m) - X_{n(i,m)}(m)\|} \end{aligned} \quad (5)$$

where $X_i(m)$ and $X_{n(i,m)}(m)$ are the time-delay embeddings with $i = 1, 2, \dots, N - (m - 1)\tau$ and $n(i, m) = 1 \leq n(i, m) \leq N - m\tau$. From Eq. 5, it can be seen that $E(m)$ is only dependent on m and τ for which $E_1(m)$ is defined as

$$E_1(m) = \frac{E(m+1)}{E(m)}. \quad (6)$$

$E_1(m)$ is therefore considered to investigate the variation from m to $m + 1$ in order to find the minimum embedding dimension m_0 (Eq. 6). As described in²⁶: " $E_1(m)$ stops changing when m is greater than some m_0 , if the time series comes from a multidimensional state space then $m_0 + 1$ is the minimum dimension". Additionally, Cao proposed $E_2(m)$ to distinguish deterministic signals from stochastic signals. $E_2(m)$ is defined as

$$E_2(m) = \frac{E^*(m+1)}{E^*(m)}, \quad (7)$$

where

$$E^*(m) = \frac{1}{N-m\tau} \sum_{i=1}^{N-m\tau} |X_i(m+1) - X_{n(i,m)}(m+1)|. \quad (8)$$

For instance, when the signal comes from random noise (values that are independent from each other), all $E_2(m)$ values are approximately equal to 1 (e.g. $E_2(m) \approx 1$). However, for deterministic data $E_2(m)$ is not constant for all m (e.g. $E_2(m) \neq 1$).

As an example of the use of $E_1(m)$ and $E_2(m)$ values, we consider two time series: the solution for the x variable of the Lorenz system (Fig 12E), and a Gaussian noise time series with zero mean and a variance of one (Fig 12F). We then compute $E_1(m)$ and $E_2(m)$ values for each time series. The $E_1(m)$ values for the chaotic time series appear to be constant after the dimension is equal to six. The determination of six is given that any value of m can be used as they are within the threshold of 1 ± 0.05 (Fig 12A). $E_2(m)$ values, for chaotic time series, are different to one (Fig 12C), for which, it can be concluded that for the chaotic time series the minimum embedding dimension the time series comes from a deterministic signal. With regard to the noise time series, $E_1(m)$ values appeared to be constant when m is close to thirteen, which is defined by the threshold of 1 ± 0.05 (Fig 12B). $E_1(m)$ values then indicate the minimum embedding dimension of the noisy time series is thirteen, however

all of the $E_2(m)$ values are approximately equal to one (Figure 12D) for which it can be concluded that noise time series is a stochastic signal.

It is important to note that for this work not only $E_1(m)$ and $E_2(m)$ are computed but also a variation of τ from 1 to 20 is presented. The purpose of such variation for τ is to show its independence with regard to $E_1(m)$ and $E_2(m)$ values as τ is increasing (Fig 12A,B,C, and D). However, one negative of the Cao's algorithm²⁶ is the definition of a new threshold where m values appear to be constant in $E_1(m)$. In the case of the given examples and reported results, we defined such threshold as 0.05. Further investigation is required for the selection of the threshold in the $E_1(m)$, as the selection of the threshold in this work is base on no particular method but visual inspection.

Average Mutual Information

When selecting the delay dimension parameter, τ , one can consider the following two cases: (i) when τ is too small, the elements of time-delay embedding will be along the bisectrix of the phase space and the reconstruction is generally not satisfactory, (ii) on the contrary, when τ is too large the elements of the uniform time-delay embedding will become spread and uncorrelated which makes recovering the underlying attractor more difficult if not impossible^{21,27,28}. With regard to the algorithms to compute τ , Emrani et al.²⁷, for instance, used the autocorrelation function in which the first zero crossing is considered as the minimum delay embedding parameter. However, the autocorrelation function is a linear statistic over which the Average Mutual Information (AMI) algorithm is preferred because the AMI takes into account the nonlinear dynamical correlations^{20,29}. With this in mind, the AMI algorithm is described below to estimate the minimum delay embedding parameter, τ_0 .

To compute the AMI, an histogram of $x(n)$ using n bins is calculated and then a probability distribution of data is computed¹⁴. AMI is therefore denoted by $I(\tau)$ which is the average mutual information between the original time series, $x(n)$, and the delayed time series, $x(n - \tau)$, delayed by τ^{30} . AMI is defined by

$$I(\tau) = \sum_{i,j}^N p_{ij} \log_2 \frac{p_{ij}}{p_i p_j}. \quad (9)$$

Probabilities are defined as follows: p_i is the probability that $x(n)$ has a value inside the i -th bin of the histogram, p_j is the probability that $x(n + \tau)$ has a value inside the j -th bin of the histogram and $p_{ij}(\tau)$ the probability that $x(n)$ is in bin i and $x(n + \tau)$ is in bin j . The AMI is measured in bits (base 2, also called shannons)^{14,31}. For small τ , AMI will be large and it will then decrease more or less rapidly. As τ increase and goes to a large limit, $x(n)$ and $x(n + \tau)$ have nothing to do with each other and p_{ij} is factorised as $p_i p_j$ for which AMI is close to zero. Then, in order to obtain τ_0 , "it has to be found the first minimum of $I(\tau)$ where $x(n + \tau)$ adds maximal information to the knowledge from $x(n)$, or, where the redundancy is the least"¹⁴.

For example, we compute the AMI for two time series: A) the x solution of the Lorenz system, and B) a noise time series using a normal distribution with mean zero and standard deviation equal to one. From Fig 13, it can then be concluded that the amount of knowledge for any noise time series is zero for which the first minimum embedding parameter is $\tau_0 = 1$. On the contrary, the first minimum of the AMI for the chaotic time series is $\tau_0 = 17$ which is the value that maximize the independence between $x(n)$ and $x(n + \tau)$ in the reconstructed state space¹⁰. Similarly as Cao's algorithm negatives, AMI's algorithm is not an exception for negatives, which are worthwhile to mention for further investigations. For instance, (i) is not clear why the choose of the first minimum of the AMI is the minimum delay embedding parameter¹⁴ and (ii) the probability distribution of the AMI function is computed with the use of histograms which depends on a heuristic choice of number of bins for which AMI depends on partitioning²⁸.

Recurrence Quantification

Recurrence Plots

Originally, Henri Poincaré in 1890 introduced the concept of recurrences in conservative systems, however such discovery was not put into practice until the development of faster computers³², for which Eckmann et al.³³ in 1987 introduced a method where recurrences in the dynamics of a system can be visualised using Recurrence Plots. The intention of Eckmann et al.³³ was to propose a tool, called Recurrence Plot (RP), that provides insights into high-dimensional dynamical systems where trajectories are very difficult to visualise. Therefore, "RP helps us to investigate the m -dimensional phase space trajectories through a two-dimensional representation of its recurrences"³⁴. Similarly, Marwan et al.³⁴ pointed out that additionally to the methodologies of the state space reconstruction and other dynamic invariants such as Lyapunov exponent, Kolmogorov-Sinai entropy, the recurrences of the trajectories in the phase space can provide important clues to characterise natural process that present, for instance, periodicities (as Milankovitch cycles) or irregular cycles (as El Niño Southern Oscillation). Such recurrences can not only be presented visually using Recurrence Plots (RP) but also be quantified with Recurrence Quantification metrics, which leads to applications of these in various areas such as economy, physiology, neuroscience, earth science, astrophysics and engineering³².

For the creation of a recurrence plot based on time series $\{x_n\}$, it is first computed the state space reconstruction with uniform time-delay embedding $X(i) = \{\tilde{x}_n, \dots, \tilde{x}_{n-(m-1)\tau}\}$ where $i = 1, \dots, N$, N is the number of considered states of $X(i)$ and $X(i) \in \mathbb{R}^m$ ³³. The recurrence plot is therefore a two-dimensional $N \times N$ square matrix, \mathbf{R} , where a black dot is placed at (i, j) whenever $X(i)$ is sufficiently close to $X(j)$:

$$\mathbf{R}_{i,j}^m(\varepsilon) = \Theta(\varepsilon_i - ||X(i) - X(j)||) \quad (10)$$

where $i, j = 1, \dots, N$, ε is a threshold distance, $||\cdot||$ a norm, and $\Theta(\cdot)$ is the Heaviside function (i.e. $\Theta(x) = 0$, if $x < 0$, and $\Theta(x) = 1$ otherwise) (Fig 14)³²⁻³⁴. RP is also characterised with a line of identity (LOI) which is a diagonal line due to $R_{i,j} = 1$ ($i, j = 1, \dots, N$).

Structures of Recurrence Plots

Pattern formations in the RPs can be designated either as topology for large-scale patterns or texture for small-scale patterns. In the case of topology, the following pattern formations are commonly presented: (i) homogeneous where uniform recurrence points are spread in the RP e.g., uniformly distributed noise (Fig 15A), (ii) periodic and quasi-periodic systems where diagonal lines and checkerboard structures represent oscillating systems, e.g., sinusoidal signals (Fig 15B), (iii) drift where paling or darkening recurrence points away from the LOI is caused by drifting systems, e.g., logistic map (Fig 15C), and (iv) disrupted where recurrence points are presented white areas or bands that indicate abrupt changes in the dynamics, e.g. Brownian motion (Fig 15D)^{33,34}. Texture patterns in RPs can be categorised as: (i) single or isolated recurrence points that represent rare occurring states, and do not persist for any time or fluctuate heavily, (ii) dots forming diagonal lines where the length of the small-scale parallel lines in the diagonal are related to the ratio of determinism or predictability in the dynamics of the system, and (iii) dots forming vertical and horizontal lines where the length of the lines represent a time length where a state does not change or change very slowly and these patterns formation represent discontinuities in the signal, and (iv) dots clustering to inscribe rectangular regions which are related to laminar states or singularities³⁴.

Although, each of the previous pattern descriptions of the structures in the RP offer an idea of the characteristics of dynamical systems, these might be misinterpreted and conclusions might tend to be subjective as these require the interpretation of a particular researcher(s). Because of that, recurrence quantification analysis (RQA) offer objective methodologies to quantify such visual characteristics of previous recurrent pattern structures in the RP³⁵.

Recurrence Quantifications Analysis (RQA)

Originally, Zbilut et al.³⁵ proposed metrics to investigate the density of recurrence points in RPs, then histograms of lengths for diagonal lines in RPs were studied by³⁶ which were the introduction to the term recurrence quantification analysis (RQA)³⁷. RQA has been applied in many fields such as life science, engineering, physics, and others³⁷. Particularly in human movement to investigate noise and complexity of postural control³⁸, postural control³⁹ or interpersonal coordination⁴⁰. The success of RQA is not only due to its simple algorithmic implementation but also to its capacity to detect tiny modulations in frequency or phase which are not detectable using standard methods e.g. spectral or wavelet analysis⁸, and that RQA's metrics are quantitatively and qualitatively independent of embedding dimension which is verified experimentally by¹². RQA metrics comprehend percentage of recurrence, percentage of determinism, ratio, Shannon entropy of the frequency distributions of the line lengths, maximal line length and divergence, trend and laminarity^{32,34}. For this work, we considered only four RQA metrics, due to its consistency with our preliminary experiments, which are described below. Such metrics are computed the nonlinearTseries R package³¹.

REC values

The percentage of recurrence (REC) is defined as

$$REC(\varepsilon, N) = \frac{1}{N^2 - N} \sum_{i \neq j=1}^N \mathbf{R}_{i,j}^m(\varepsilon), \quad (11)$$

which enumerates the black dots in the RP excluding the line of identity. REC is a measure of the relative density of recurrence points in the sparse matrix³⁴.

DET values

The percent determinism (DET) is defined as the fraction of recurrence points that form diagonal lines and it is determined by

$$DET = \frac{\sum_{l=d_{min}}^N l H_D l}{\sum_{i,j=1}^N \mathbf{R}_{i,j}^m(\varepsilon)}, \quad (12)$$

where

$$H_D(l) = \sum_{i,j=1}^N (1 - \mathbf{R}_{i-1,j-1}(\varepsilon))(1 - \mathbf{R}_{i+l,j+l}(\varepsilon)) \prod_{k=0}^{l-1} \mathbf{R}_{i+k,j+k}(\varepsilon) \quad (13)$$

is the histogram of the lengths of the diagonal structures in the RP. DET can be interpreted as the predictability of the system for periodic signals which, in essence, have longer diagonal lines than the short diagonals lines for chaotic signals or absent diagonal lines for stochastic signals^{32,34}. Similarly, DET is considered as a measurement for the organisation of points in RPs¹².

RATIO values

RATIO is defined as the ratio between DET and REC and it is calculated from the frequency distributions of the lengths of the diagonal lines. RATIO is useful to discover dynamic transitions³⁴.

ENT values

ENT is the Shannon entropy of the frequency distribution of the diagonal line lengths and it is defined as

$$ENT = - \sum_{l=d_{min}}^N p(l) \ln p(l) \quad \text{with} \quad p(l) = \frac{H_D(l)}{\sum_{l=d_{min}}^N H_D(l)}. \quad (14)$$

ENT reflects the complexity of the deterministic structure in the system. For instance, for uncorrelated noise or oscillations, the value of ENT is rather small and indicates low complexity of the system, therefore "the higher the ENT is the more complex the dynamics are"^{32,34}.

Sensitivity and robustness of RPs and RQA.

RP and RQA are a very young field in nonlinear dynamics and many questions are still open, for instance, different parameters for window length size of the time series, embedding parameters or recurrence threshold can generate different results in RQA's metrics^{8,33}.

The selection of recurrence threshold, ε , can depend on the system that is analysed. For instance, when studying dynamical invariants ε require to be very small, for trajectory reconstruction ε requires to have a large thresholds or when studying dynamical transition there is little importance about the selection of the threshold⁸. Other criteria for the selection of ε is that the recurrence threshold should be five times larger than the standard deviation of the observational noise or the use of diagonal structures within the RP is suggested in order to find the optimal recurrence threshold for (quasi-)periodic process⁸. Similarly, Iwanski et al.¹² highlighted the importance of choosing the right embedding parameters to perform RQA for which many experiments have to be performed using different parameters in order to have a better intuition of the nature of the time series and how this is represented by using RQA.

With that in mind, this work explores the sensitivity and robustness of the window size of time series, embedding parameters for RSS with UTDE and recurrence threshold for RP and RQA in order to gain a better insight into the underlying time series collected from inertial sensors in the context of human-humanoid imitation activities.

Experiment

We conducted an experiment in the context of human-humanoid imitation (HHI) activities where participants were asked to imitate simple horizontal and vertical arm movements performed by NAO, a humanoid robot². Such simple movements were repeated ten times for the participant who copied NAO's arm movements in a face-to-face imitation activity. Also, wearable inertial measurement unit (IMU) sensors were attached to the right hand of the participant and to the left hand of the robot (Figure 16 A,C). Data were then collected with four NeMEMSi IMU sensors with sampling rate of 50Hz providing tri-axial data of the accelerometer, gyroscope and magnetometer sensors and quaternions⁴¹.

Ethics

The experiments of this work were conducted in November 2016 and participants confirmed reading and understanding the participant information sheet of the experiments and were able to withdraw from the experiment at any time without giving any reason. The design of the experiments adhered to the University of X regulations, data were anonymised and videos were stored only on a personal computer in accordance with the Data Protection Act 1998.

Participants

Twenty-three participants, from now on defined as pN where N is the number of participant, were invited to do the experiment. However, data for three participants were not used because the instructions for $p01$, who was the only left-handed, were mistakenly given in a way that movements were performed different from what had been planned, and for participants $p13$ and $p16$ data were corrupted because bluetooth communications problems with the sensors. With that in mind, data for twenty participants were analysed in this work.

Of the twenty participants, all of them are right-handed healthy participants of whom four are females and sixteen are males with a mean and standard deviation (SD) age of mean=19.8 (SD=1.39). All participants provided informed consent forms prior to participation in the experiment.

Human-humanoid imitation activities

For human-humanoid imitation (HHI) activities four neMEMSi sensors were used, two of which were attached to the right hand of the participant and the other two to the left hand of the humanoid robot. Then, each participant was asked to imitate repetitions of simple horizontal and vertical arm movements performed by the humanoid robot in the following conditions: (i) ten repetitions of horizontal arm movement at normal (HN) and faster (HF) speed (Figure 16 A), and (ii) ten repetitions of vertical arm movement at normal (VN) and faster (VF) speed (Figure 16 C). The normal and faster speed of arm movements is defined by the duration in number of samples of one repetition of NAO's arm movements. We select NAO's arm movements duration to distinguish between normal and faster arm movements as NAO's movements have less variation between repetition to repetition. The duration for one repetition of the horizontal arm movement at normal speed, HN, is about 5 seconds considering that each repetition last around 250 samples. For horizontal arm movement at faster speed, HF, each repetition were performed in around 2 seconds which correspond to 90 samples of data. The vertical arm movement at normal speed, VN, were performed in 6 seconds which is around 300 samples of data. For vertical arm movement at faster speed, VF, each repetition lasts about 2.4 seconds which correspond to 120 samples of data. To visualise the distinction between normal and faster speed for horizontal and vertical arm movements, Fig 17 shows smoothed time series for axes Z and Y of the gyroscope sensors with four window lengths: 2-sec (100-samples), 5-sec (250-samples), 10-sec (500-samples) and 15-sec (750-samples).

Data from Inertial Measurement Units

To give insight to the research questions, we considered various conditions of time series collected for this work (see Experiment section for more details) which are described as follows

- Three levels of smoothness for the normalised data ($sg0zmuv$, $sg1zmuv$ and $sg2zmuv$), computed from two different filter lengths (29 and 159) with the same polynomial degree of 5 using the function `sgolay(p, n, m)`⁴²,
- four velocities arm movement activities: horizontal normal (HN), horizontal faster (HF), vertical normal (VN), and vertical faster (VF), and
- four window lengths: 2-sec (100 samples), 5-sec (250 samples), 10-sec (500 samples) and 15-sec (750 samples).

After the data collection, raw time series were windowed, normalised and smoothed. Then, due to space limitations and to have simple visualisation, we only present 10-sec (500 samples) window length time series for three participants ($p01$, $p01$ and $p03$) performing horizontal arm movements (axis GyroZ) and vertical arm movements (axis GyroY) (Figs 18).

Raw data

Considering the work of⁴³ which provided evidence of an improvement in recognition activities when combining data from accelerometer and gyroscope. We focus our analysis from data of the accelerometer and gyroscope of the NeMEMSi sensors⁴¹ and leave the data of the magnetometer and quaternions for further investigation because of their possible variations with regard to magnetic disturbances.

Data from the accelerometer is defined by triaxial time series $A_x(n)$, $A_y(n)$, $A_z(n)$ which forms the matrix A (Eq. 15), and the same for data from the gyroscope which is defined by triaxial time-series of $G_x(n)$, $G_y(n)$, $G_z(n)$ representing the matrix G (Eq. 16). Both triaxial time series of each sensor, a and g , are denoted with its respective axes subscripts x, y, z , where n is the sample index and N is the same maximum length of all axes for the time series. Matrices A and G are represented as follows

$$A = \begin{pmatrix} A_x(n) \\ A_y(n) \\ A_z(n) \end{pmatrix} = \begin{pmatrix} a_x(1), a_x(2), \dots, a_x(N) \\ a_y(1), a_y(2), \dots, a_y(N) \\ a_z(1), a_z(2), \dots, a_z(N) \end{pmatrix}, \quad (15)$$

and

$$G = \begin{pmatrix} G_x(n) \\ G_y(n) \\ G_z(n) \end{pmatrix} = \begin{pmatrix} g_x(1), g_x(2), \dots, g_x(N) \\ g_y(1), g_y(2), \dots, g_y(N) \\ g_z(1), g_z(2), \dots, g_z(N) \end{pmatrix}. \quad (16)$$

Postprocessing data

After the collection of raw data from four NeMEMSi sensors, time synchronisation alignment and interpolation were performed in order to create time series with the same length and synchronised time. We refer the reader to⁴¹ for further details about the time synchronisation process.

Data normalization

Data is normalised to have zero mean and unit variance using sample mean and sample standard deviation. The sample mean and sample standard deviation using $x(n)$ is given by

$$\mu_{x(n)} = \frac{1}{N} \left(\sum_{i=1}^N x(i) \right), \quad \sigma_{x(n)} = \sqrt{\frac{\sum_{i=1}^N (x(i) - \mu_{x(n)})^2}{N-1}}, \quad (17)$$

and the normalised data, $\hat{x}(n)$, is computed as follows

$$\hat{x}(n) = \frac{x(n) - \mu_{x(n)}}{\sigma_{x(n)}}. \quad (18)$$

Smoothing data

Commonly, a low-pass filter is the method either to capture the low frequencies that represent %99 of the human body energy or to get the gravitational and body motion components of accelerations⁴⁴. However, for this work the elimination of certain range of frequencies is not the main focus but the conservation of the structure in the time series in terms of the width and heights where, for instance, Savitzky-Golay filter can help to accomplish such task⁴⁵. Savitzky-Golay filter is based on the principle of moving window averaging which preserves the area under the curve (the zeroth moment) and its mean position in time (the first moment) but the line width (the second moment) is violated and that results, for example, in the case of spectrometric data where a narrow spectral line is presented with reduced height and width. With that in mind, the aim of Savitzky-Golay filtering is to find filter coefficients c_n that preserve higher momentums which are based on local least-square polynomial approximations^{45–47}. Therefore, Savitzky-Golay coefficients are therefore computed using an R function `sgolay(p, n, m)` where p is the filter order, n is the filter length (must be odd) and m is the m -th derivative of the filter coefficients⁴². Smoothed signal is represented with a tilde over the original signal: $\tilde{x}(n)$.

Window size data

With regard to the window size,⁴³ investigated its effects using seven window lengths (2, 5, 10, 15, 20, 25, 30 seconds) and combination of inertial sensors (accelerometer, gyroscope and linear acceleration sensor) to improve the activity recognition performance for repetitive activities (walking, jogging and biking) and less repetitive activities (smoking, eating, giving a talk or drinking a coffee). With that in mind, Shoaib et al.⁴³ concluded that the increase of window length improve the recognition of complex activities because these requires a large window length to learn the repetitive motion patterns. Particularly, one of the recommendations is to use large window size to recognise less repetitive activities which mainly involve random hand gestures. Therefore, for the four activities (HN, HF, VN, and VF) in this work, which are mainly repetitive, we select only four window sizes for analysis: 2-s window (100 samples), 5-s window (250 samples), 10-s (500 samples) and 15-s window (750 samples) (Fig 17).

References

1. Davids, K., Glazier, P., Araújo, D. & Bartlett, R. Movement systems as dynamical systems. *Sports Medicine* **33**, 245–260, DOI: [10.2165/00007256-200333040-00001](https://doi.org/10.2165/00007256-200333040-00001) (2003).
2. Gouaillier, D. et al. Mechatronic design of nao humanoid. In *Proceedings of the 2009 IEEE International Conference on Robotics and Automation, ICRA'09*, 2124–2129 (IEEE Press, Piscataway, NJ, USA, 2009).
3. Quintana Duque, J. C. Non-linear dynamic invariants based on embedding reconstruction of systems for pedaling motion. In Byshko, R. (ed.) *Sportinformatik 2012 : 9. vom 12.- 14. Sept. 2012 in Konstanz : Beiträge*, 28–38 (Universität, 2012).
4. Quintana Duque, J. C. *Non-linear methods for the quantification of cyclic motion*. PhD dissertation, University of Konstanz, Konstanz, Germany (2016).
5. Samà, A. et al. Gait identification by means of box approximation geometry of reconstructed attractors in latent space. *Neurocomputing* **121**, 79–88, DOI: [10.1016/j.neucom.2012.12.042](https://doi.org/10.1016/j.neucom.2012.12.042) (2013).
6. Frank, J., Mannor, S. & Precup, D. Activity and gait recognition with time-delay embeddings. *AAAI Conf. on Artif. Intell.* 407–408 (2010).

7. Gómez-García, J. A., Godino-Llorente, J. I. & Castellanos-Domínguez, G. Non uniform embedding based on relevance analysis with reduced computational complexity: Application to the detection of pathologies from biosignal recordings. *Neurocomputing* **132**, 148 – 158 (2014). Innovations in Nature Inspired Optimization and Learning Methods Machines learning for Non-Linear Processing.
8. Marwan, N. How to Avoid Potential Pitfalls in Recurrence Plot Based Data Analysis. *Int. J. Bifurc. Chaos* **21**, 1003, DOI: [10.1142/S0218127411029008](https://doi.org/10.1142/S0218127411029008) (2011). [1007.2215](#).
9. Stergiou, N. & Decker, L. M. Human movement variability, nonlinear dynamics, and pathology: Is there a connection? *Hum. Mov. Sci.* **30**, 869 – 888 (2011). EWOMS 2009: The European Workshop on Movement Science.
10. Bradley, E. & Kantz, H. Nonlinear time-series analysis revisited. *Chaos: An Interdiscip. J. Nonlinear Sci.* **25**, 097610, DOI: [10.1063/1.4917289](https://doi.org/10.1063/1.4917289) (2015).
11. Takens, F. Detecting strange attractors in turbulence. *Dyn. Syst. Turbul. Warwick 1980: Proc. a Symp. Held at Univ. Warwick 1979/80* 366–381 (1981).
12. Iwanski, J. S. & Bradley, E. Recurrence plots of experimental data: To embed or not to embed? *Chaos: An Interdiscip. J. Nonlinear Sci.* **8**, 861–871, DOI: [10.1063/1.166372](https://doi.org/10.1063/1.166372) (1998). <https://doi.org/10.1063/1.166372>.
13. Garland, J., Bradley, E. & Meiss, J. D. Exploring the topology of dynamical reconstructions. *Phys. D: Nonlinear Phenom.* **334**, 49 – 59 (2016). Topology in Dynamics, Differential Equations, and Data.
14. Kantz, H. & Schreiber, T. *Nonlinear Time Series Analysis* (Cambridge University Press, New York, NY, USA, 2003).
15. Xochicale, M. *Github repository: Recurrent Quantification Analysis of Human-Humanoid Interaction Activities* (2020). <https://github.com/mxochicale/srep2020>.
16. Packard, N. H., Crutchfield, J. P., Farmer, J. D. & Shaw, R. S. Geometry from a time series. *Phys. Rev. Lett.* **45**, 712–716, DOI: [10.1103/PhysRevLett.45.712](https://doi.org/10.1103/PhysRevLett.45.712) (1980).
17. Aguirre, L. A. & Letellier, C. Modeling nonlinear dynamics and chaos: A review. *Math. Probl. Eng.* **11**, 1–22 (2009).
18. Guastello, S. J. & Gregson, R. A. M. *Nonlinear Dynamical Systems Analysis for the Behavioral Science Using Real Data* (CRC Press, 2011).
19. Quintana-Duque, J. & Saupe, D. *Evidence of Chaos in Indoor Pedaling Motion using Non-linear Methods*. July (Routledge, 2013).
20. Krakovská, A., Mezeiová, K. & I, H. B. Use of False Nearest Neighbours for Selecting Variables and Embedding Parameters for State Space Reconstruction. *J. Complex Syst.* **2015** (2015).
21. Casdagli, M., Eubank, S., Farmer, J. & Gibson, J. State space reconstruction in the presence of noise. *Phys. D: Nonlinear Phenom.* **51**, 52 – 98 (1991).
22. Gibson, J. F., Farmer, J. D., Casdagli, M. & Eubank, S. An analytic approach to practical state space reconstruction. *Phys. D: Nonlinear Phenom.* **57**, 1 – 30 (1992).
23. Uzal, L. C., Grinblat, G. L. & Verdes, P. F. Optimal reconstruction of dynamical systems: A noise amplification approach. *Phys. Rev. E* **84**, 016223, DOI: [10.1103/PhysRevE.84.016223](https://doi.org/10.1103/PhysRevE.84.016223) (2011).
24. Uzal, L. C. & Verdes, P. F. Optimal Irregular Delay Embeddings. In *Dynamics Days South America 2010* (National Institute for Space Research, 2010).
25. Kennel, M. B., Brown, R. & Abarbanel, H. D. I. Determining embedding dimension for phase-space reconstruction using a geometrical construction. *Phys. Rev. A* **45**, 3403–3411, DOI: [10.1103/PhysRevA.45.3403](https://doi.org/10.1103/PhysRevA.45.3403) (1992).
26. Cao, L. Practical method for determining the minimum embedding dimension of a scalar time series. *Phys. D: Nonlinear Phenom.* **110**, 43–50 (1997).
27. Emrani, S., Gentimis, T. & Krim, H. Persistent homology of delay embeddings and its application to wheeze detection. *IEEE Signal Process. Lett.* **21**, 459–463, DOI: [10.1109/LSP.2014.2305700](https://doi.org/10.1109/LSP.2014.2305700) (2014).
28. Garcia, S. P. & Almeida, J. S. Nearest neighbor embedding with different time delays. *Phys. Rev. E* **71**, 037204, DOI: [10.1103/PhysRevE.71.037204](https://doi.org/10.1103/PhysRevE.71.037204) (2005).
29. Fraser, A. M. & Swinney, H. L. Independent coordinates for strange attractors from mutual information. *Phys. Rev. A* **33**, 1134–1140 (1986).
30. Kabiraj, L., Saurabh, A., Wahi, P. & Sujith, R. I. Route to chaos for combustion instability in ducted laminar premixed flames. *Chaos: An Interdiscip. J. Nonlinear Sci.* **22**, 023129, DOI: [10.1063/1.4718725](https://doi.org/10.1063/1.4718725) (2012).

31. Garcia, C. A. & Sawitzki, G. *nonlinearTseries: Nonlinear Time Series Analysis* (2016). R package version 0.2.4 — For new features, see the 'Changelog' file (in the package source).
32. Marwan, N., Romano, M. C., Thiel, M. & Kurths, J. Recurrence plots for the analysis of complex systems. *Phys. Reports* **438**, 237 – 329, DOI: <https://doi.org/10.1016/j.physrep.2006.11.001> (2007).
33. Eckmann, J.-P., Kamphorst, S. O. & Ruelle, D. Recurrence plots of dynamical systems. *EPL (Europhysics Lett.)* **4**, 973 (1987).
34. Marwan, N. & Webber, C. L. Mathematical and computational foundations of recurrence quantifications. In Webber, C. L. & Marwan, N. (eds.) *Recurrence Quantification Analysis: Theory and Best Practices*, chap. 1, 3–43 (Springer, Cham, 2015), 1 edn.
35. Zbilut, J. P. & Webber, C. L. Embeddings and delays as derived from quantification of recurrence plots. *Phys. Lett. A* **171**, 199 – 203, DOI: [https://doi.org/10.1016/0375-9601\(92\)90426-M](https://doi.org/10.1016/0375-9601(92)90426-M) (1992).
36. Trulla, L., Giuliani, A., Zbilut, J. & Webber, C. Recurrence quantification analysis of the logistic equation with transients. *Phys. Lett. A* **223**, 255 – 260, DOI: [https://doi.org/10.1016/S0375-9601\(96\)00741-4](https://doi.org/10.1016/S0375-9601(96)00741-4) (1996).
37. Marwan, N. A historical review of recurrence plots. *The Eur. Phys. J. Special Top.* **164**, 3–12, DOI: [10.1140/epjst/e2008-00829-1](https://doi.org/10.1140/epjst/e2008-00829-1) (2008).
38. Rhea, C. K. *et al.* Noise and complexity in human postural control: Interpreting the different estimations of entropy. *PLOS ONE* **6**, 1–9, DOI: [10.1371/journal.pone.0017696](https://doi.org/10.1371/journal.pone.0017696) (2011).
39. Apthorp, D., Nagle, F. & Palmisano, S. Chaos in balance: Non-linear measures of postural control predict individual variations in visual illusions of motion. *PLOS ONE* **9**, 1–22, DOI: [10.1371/journal.pone.0113897](https://doi.org/10.1371/journal.pone.0113897) (2014).
40. Duran, N. D. & Fusaroli, R. Conversing with a devil's advocate: Interpersonal coordination in deception and disagreement. *PLOS ONE* **12**, 1–25, DOI: [10.1371/journal.pone.0178140](https://doi.org/10.1371/journal.pone.0178140) (2017).
41. Comotti, D., Galizzi, M. & Vitali, A. nememsi: One step forward in wireless attitude and heading reference systems. In *2014 International Symposium on Inertial Sensors and Systems (ISISS)*, 1–4, DOI: [10.1109/ISISS.2014.6782521](https://doi.org/10.1109/ISISS.2014.6782521) (2014).
42. signal R developers. *signal: Signal processing* (2014).
43. Shoaib, M., Bosch, S., Incel, O. D., Scholten, H. & Havinga, P. J. M. Complex human activity recognition using smartphone and wrist-worn motion sensors. *Sensors* **16**, DOI: [10.3390/s16040426](https://doi.org/10.3390/s16040426) (2016).
44. Anguita, D., Ghio, A., Oneto, L., Parra, X. & Reyes-Ortiz, J. L. A public domain dataset for human activity recognition using smartphones. In *21th European Symposium on Artificial Neural Networks, Computational Intelligence and Machine Learning, ESANN 2013*, DOI: [978-2-87419-081-0](https://doi.org/10.2390/978-2-87419-081-0) (2013).
45. Press, W. H., Teukolsky, S. A., Vetterling, W. T. & Flannery, B. P. *Numerical Recipes in C (2Nd Ed.): The Art of Scientific Computing* (Cambridge University Press, New York, NY, USA, 1992).
46. Savitzky, A. & Golay, M. J. E. Smoothing and differentiation of data by simplified least squares procedures. *Anal. Chem.* **36**, 1627–1639 (1964).
47. Schafer, R. W. On the frequency-domain properties of savitzky-golay filters. In *2011 Digital Signal Processing and Signal Processing Education Meeting (DSP/SPE)*, 54–59, DOI: [10.1109/DSP-SPE.2011.5739186](https://doi.org/10.1109/DSP-SPE.2011.5739186) (2011).

Acknowledgements

This work was funded by the University of Birmingham and the Mexican National Council of Science and Technology as part of Miguel Xochicale's PhD degree. I would like to thank to Dr. Dolores Columba Perez Flores and Prof. Martin J Russell for their helpful comments to polish the use of the language of mathematics and to Constantino Antonio Garcia Martinez *et al.* for developing the R package nonlinearTseries that help to accelerate the analysis of the nonlinear time series in this work.

Author contributions statement

Contributions for this work of Miguel Xochicale (MX) and Chris Baber (CB) are as follows:

Conceptualisation MX, CB

Data Curation MX

Formal Analysis MX

Funding Acquisition MX, CB

Investigation MX

Methodology MX

Project Administration MX

Resources CB

Software MX

Supervision CB

Validation MX

Verification MX

Writing - Original Draft Preparation MX

Writing - Review MX, CB

Writing - Editing MX

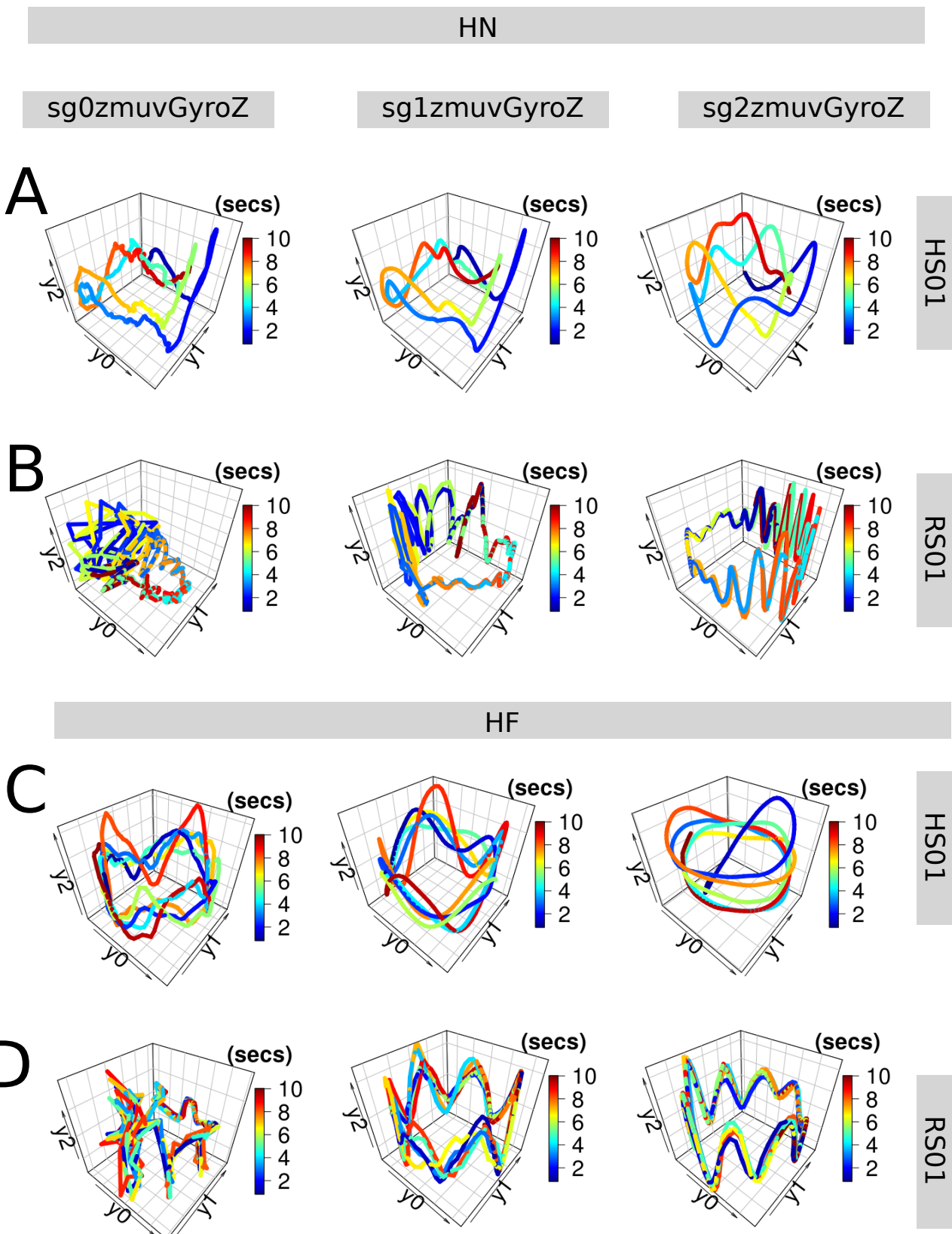


Figure 2. RSSs for horizontal arm movements. Reconstructed state spaces for time series for p01 of Figure 18. Reconstructed state spaces were computed with embedding parameters $\bar{m}_0 = 6$, $\bar{\tau}_0 = 8$. Code and data to reproduce the figure is available in [15](#).

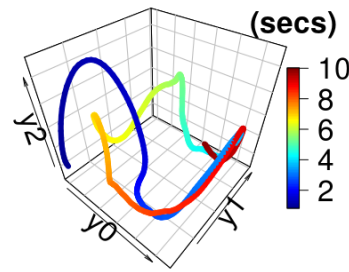
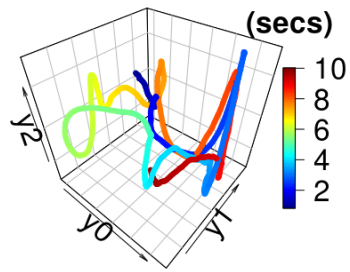
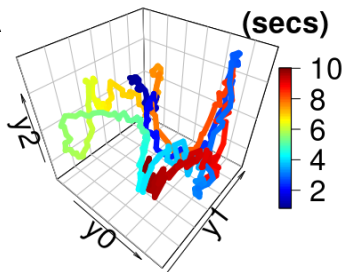


sg0zmuvGyroY

sg1zmuvGyroY

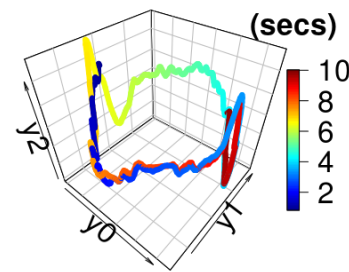
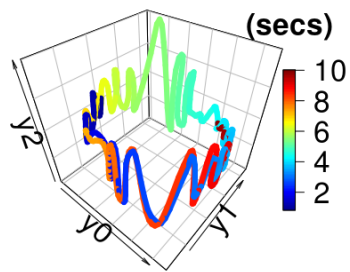
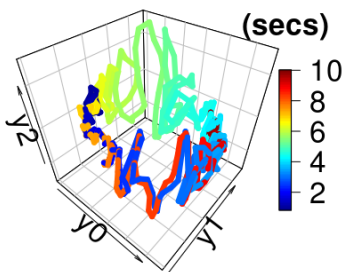
sg2zmuvGyroY

A



HS01

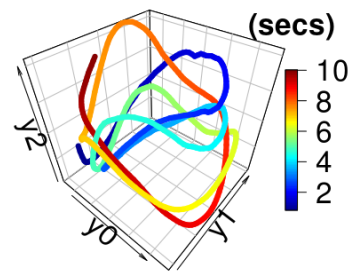
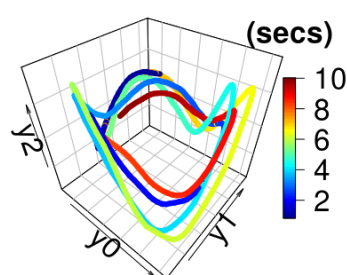
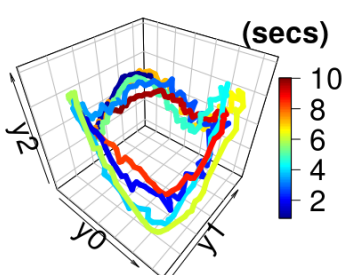
B



RS01

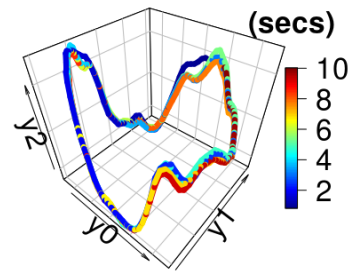
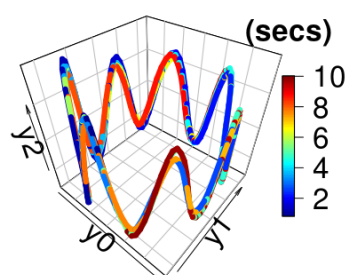
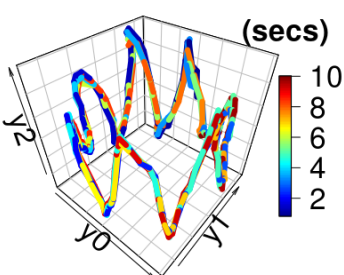
VF

C



HS01

D



RS01

Figure 3. RSSs for vertical arm movements. Reconstructed state spaces for time series for p01 of Figure 18. Reconstructed state spaces were computed with embedding parameters $\bar{m}_0 = 6$, $\bar{\tau}_0 = 8$. Code and data to reproduce the figure is available in [15](#).

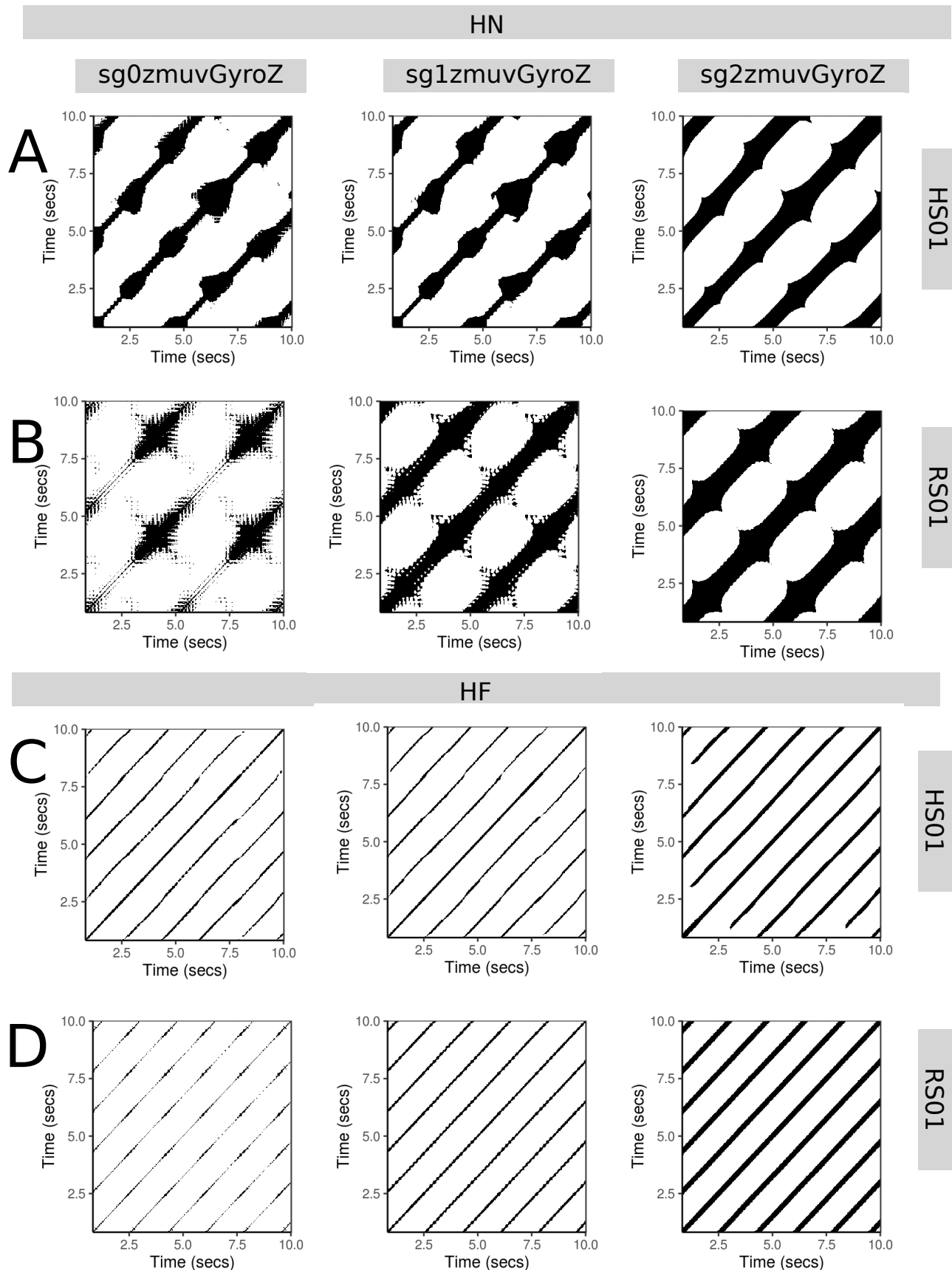


Figure 4. RPs for horizontal arm movements. Recurrence plots were computed with embedding parameters $\bar{m}_0 = 6$, $\bar{\tau}_0 = 8$, and $\varepsilon = 1$. Code and data to reproduce the figure is available in¹⁵.

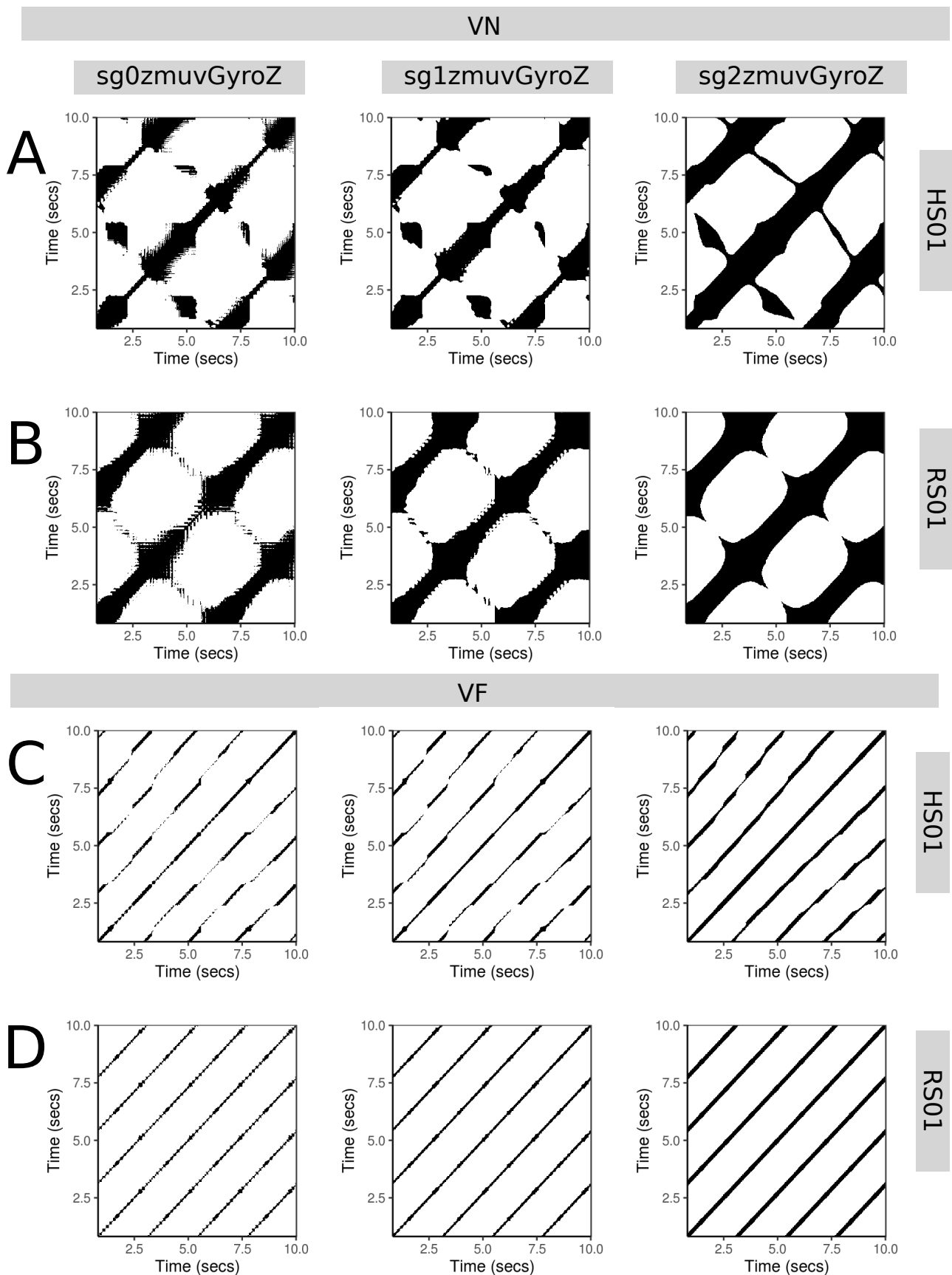


Figure 5. RPs for vertical arm movements. Recurrence plots were computed with $\bar{m}_0 = 6$, $\bar{\tau}_0 = 8$, and $\varepsilon = 1$. Code and data to reproduce the figure is available in [15](#).

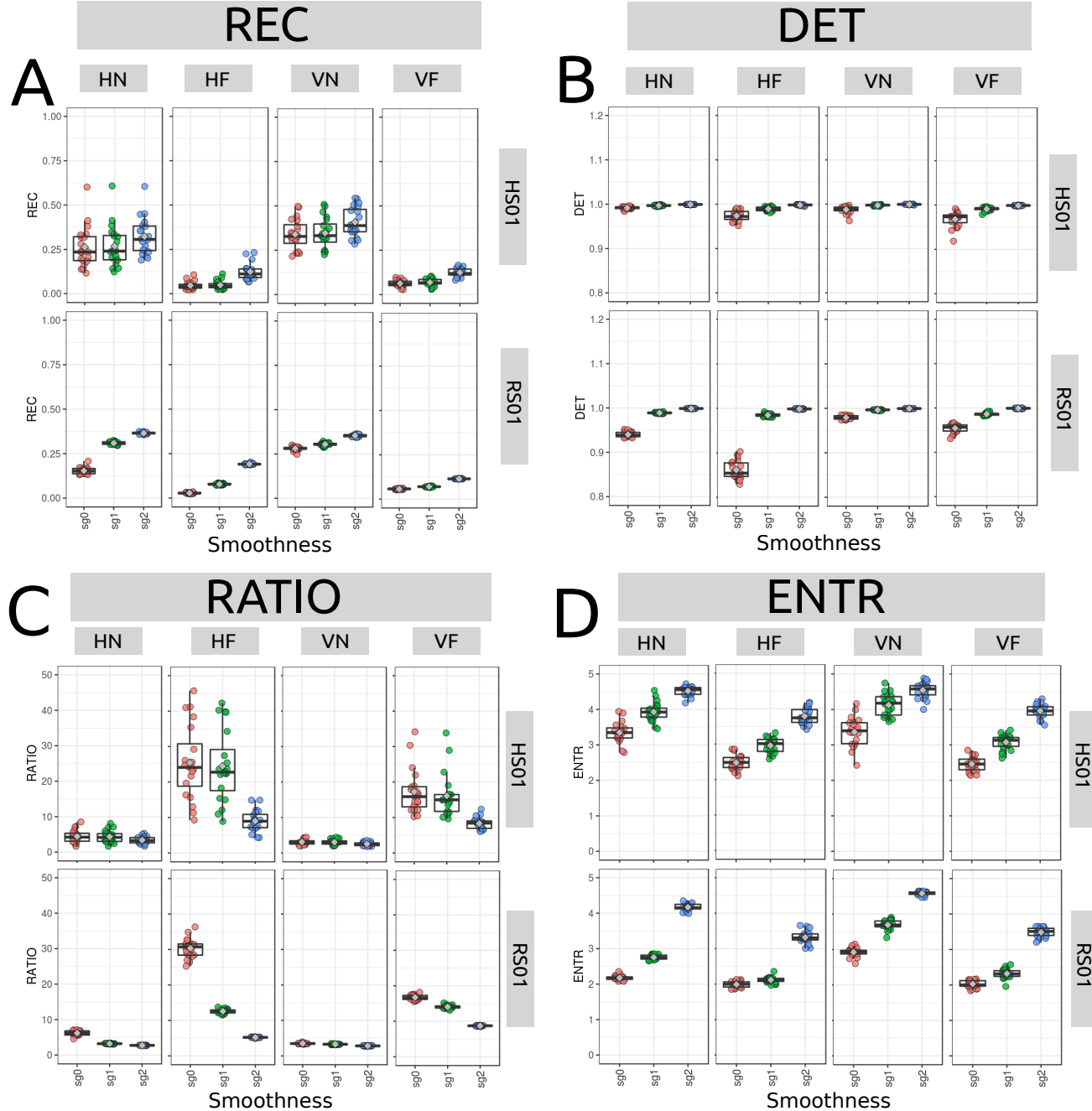


Figure 6. Box plots for RQA metrics. RQA metrics for (A) REC, (B) DET, (C) RATIO, and (D) ENTR of 20 participants performing HN, HF, VN and VF movements with sensors HS01, RS01 and three smoothed-normalised time series (sg0, sg1 and sg2). RQA values were computed with $\bar{m}_0 = 6$, $\bar{\tau}_0 = 8$, and $\varepsilon = 1$. Code and data to reproduce the figure is available in¹⁵.

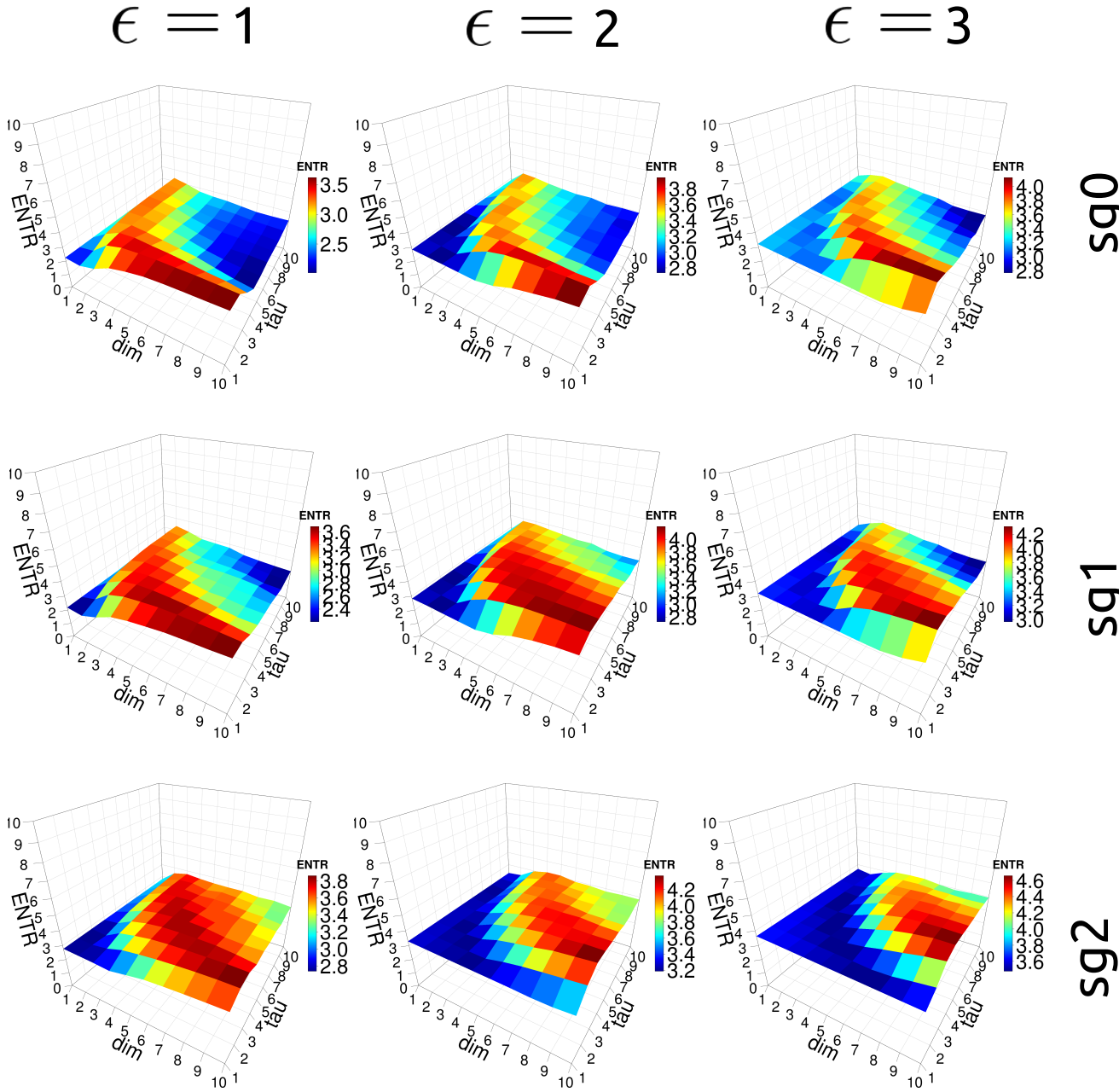


Figure 7. 3D surface plots of RQA ENTR values for different recurrence threshold and smoothness levels. RQA ENTR values are for embedding parameters $\{m \in \mathbb{R} | 0 \leq m \leq 10\}$, $\{\tau \in \mathbb{R} | 0 \leq \tau \leq 10\}$ incrementing by one and three recurrence thresholds $\epsilon = 1, 2, 3$. RQA ENTR values were computed with data from p03, sensor HS01, with a window size of 10-secs (500 samples). Code and data to reproduce the figure is available in [15](#).

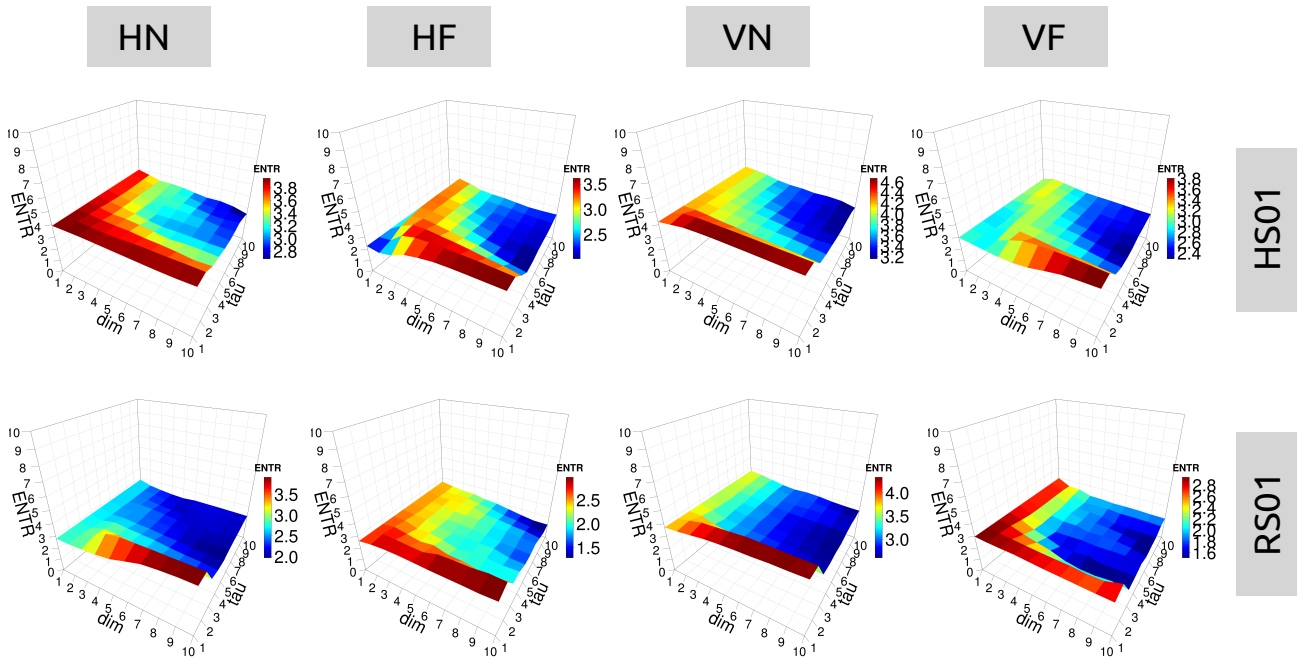


Figure 8. 3D surface plots of RQA ENTR values for different sensors and activities. RQA ENTR values are for embedding parameters $\{m \in \mathbb{R} | 0 \leq m \leq 10\}$, $\{\tau \in \mathbb{R} | 0 \leq \tau \leq 10\}$ with $\varepsilon = 1$ considering four activities Horizontal Normal (HN), Horizontal Faster(HF), Vertical Normal(VN), and Vertical Faster (VF) and sensors Human Sensor 01 (HS01) and Robot Sensor (RS01). RQA ENTR values were computed from data of $p03$, $sg0$ and window size of 10-secs (500 samples). Code and data to reproduce the figure is available in¹⁵.

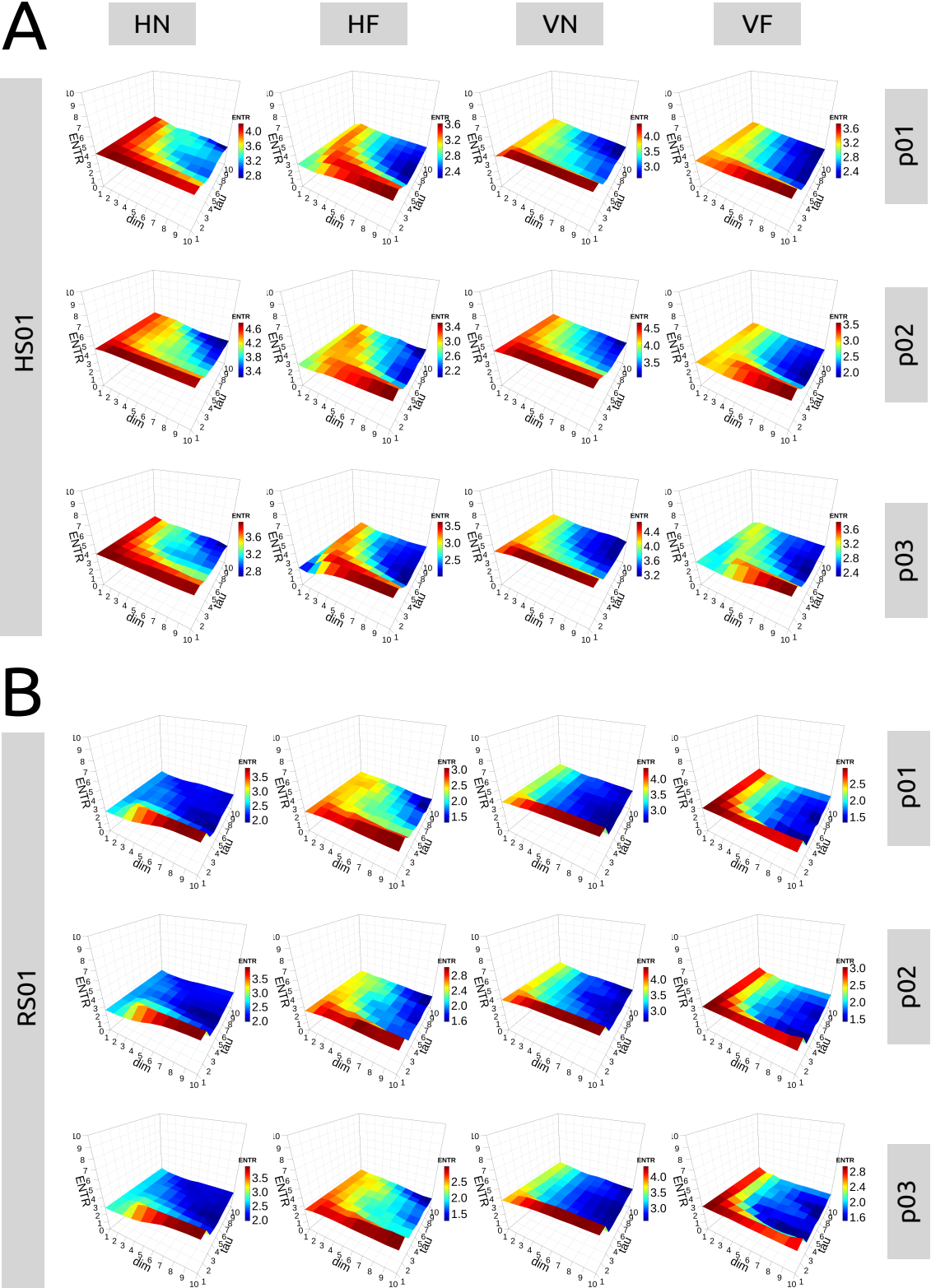


Figure 9. 3D surface plots of RQA ENTR values for different participants, activities and sensors. RQA ENTR values are for participants (p01, p02, and p03) in the categories of (A) Human Sensor 01 (HS01) and (B) Robot Sensor 01 (RS01) considering embedding parameters $\{m \in \mathbb{R} | 0 \leq m \leq 10\}$, $\{\tau \in \mathbb{R} | 0 \leq \tau \leq 10\}$ with $\varepsilon = 1$ and four activities Horizontal Normal (HN), Horizontal Faster(HF), Vertical Normal(VN), and Vertical Faster (VF). RQA ENTR values were computed from data of sg0 and window size of 10-secs (500 samples). Code and data to reproduce the figure is available in ¹⁵.

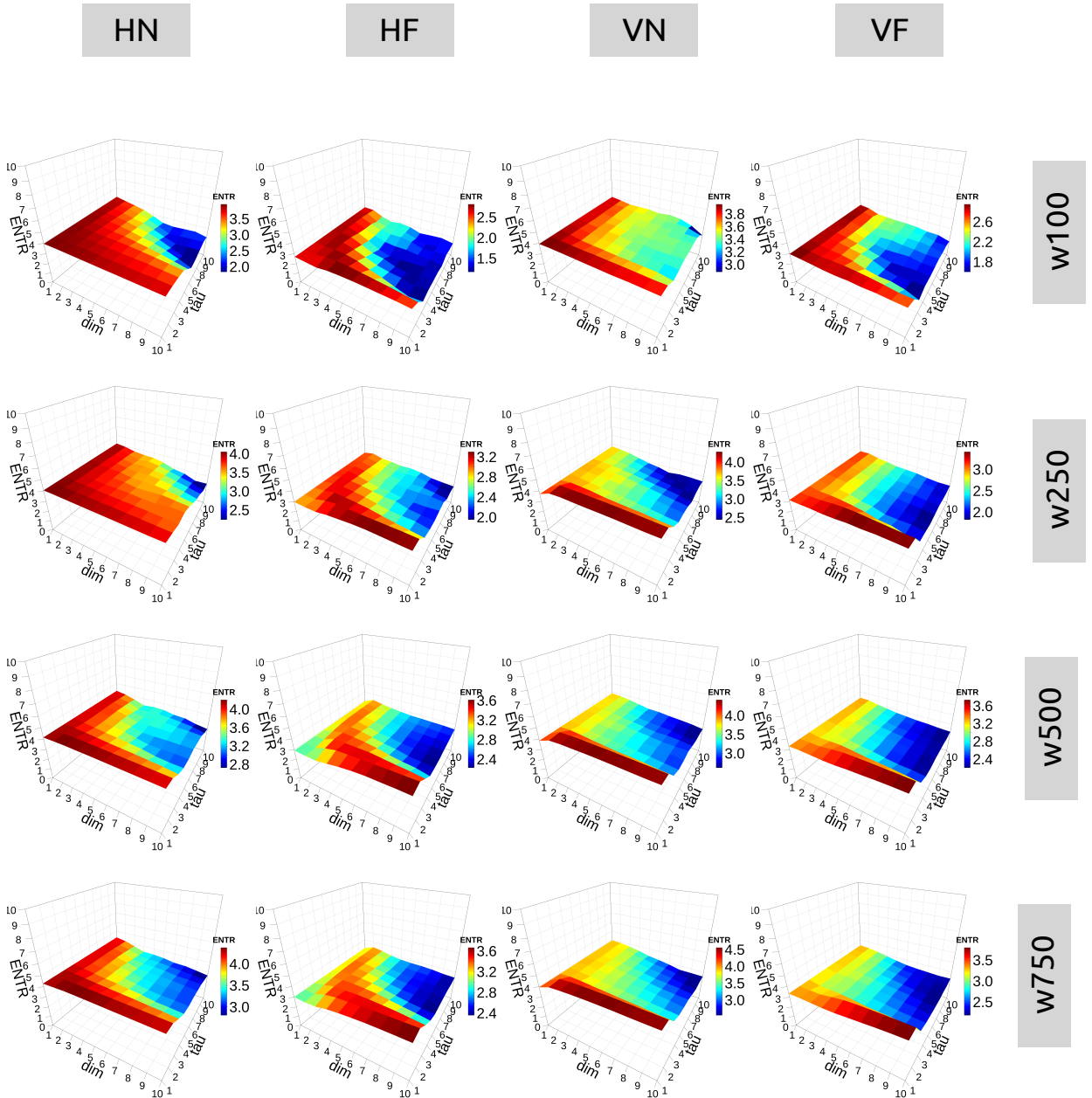


Figure 10. 3D surface plots of RQA ENTR values for different windows lengths and activities. RQA ENTR values are for embedding parameters $\{m \in \mathbb{R} | 0 \leq m \leq 10\}$, $\{\tau \in \mathbb{R} | 0 \leq \tau \leq 10\}$, with $\varepsilon = 1$ considering four windows lengths (e.g., w100 (100 samples), w250 (250 samples), w500 (500 samples) and w750 (750 samples)) and four activities Horizontal Normal (HN), Horizontal Faster(HF), Vertical Normal(VN), and Vertical Faster (VF). RQA ENTR values were computed from data of p01 and sg0. Code and data to reproduce the figure is available in¹⁵.

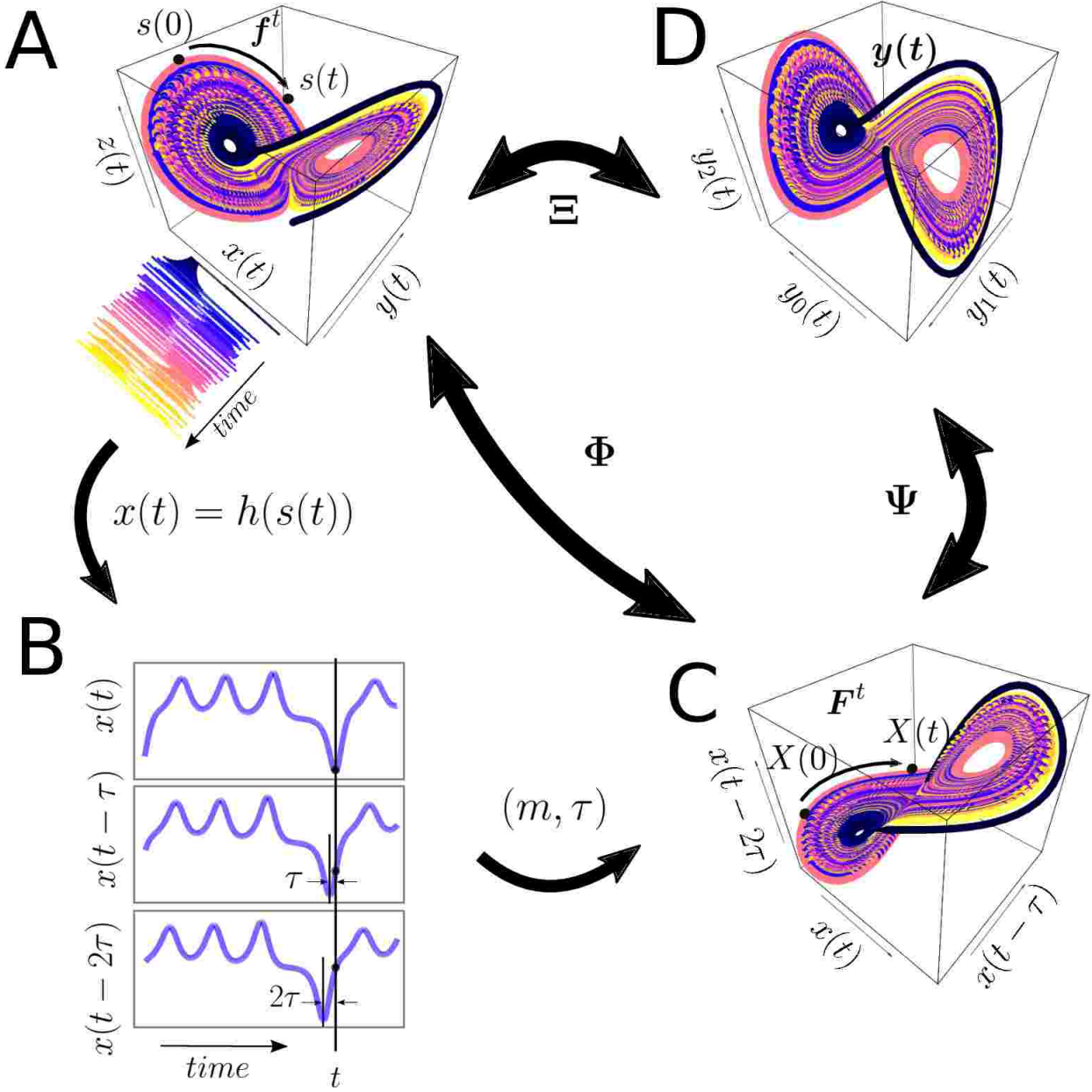


Figure 11. State space reconstruction methodology. State space reconstruction is based on $x(t) = h[s(t)] = h[f^t[s(0)]]$ where f^t is the true dynamical system, $s(t)$ indicates the state, s , at time, t , and $h[\cdot]$ the measurement function. The time-delay embedding represented as the Φ , maps the original d -dimensional state $s(t)$ into the m -dimensional uniform time-delay embedding matrix $X(t)$. The transformation map Ψ then maps $X(t)$ into a new state $y(t)$ of dimensions $n < m$. (A) M -dimensional manifold representing the state space (e.g. Lorenz system); (B) Delayed copies of 1-dimensional $x(t)$ from the Lorenz system; (C) m -dimensional reconstructed state space with m and τ , and (D) $y(t)$ is the n -dimensional reconstructed state space. The total reconstruction map is represented as $\Xi = \Psi \circ \Phi$ where Φ is the delay reconstruction map and Ψ is the coordinate transformation map. This figure is adapted from^{3,21,23}. Code and data to reproduce the figure is available in¹⁵.

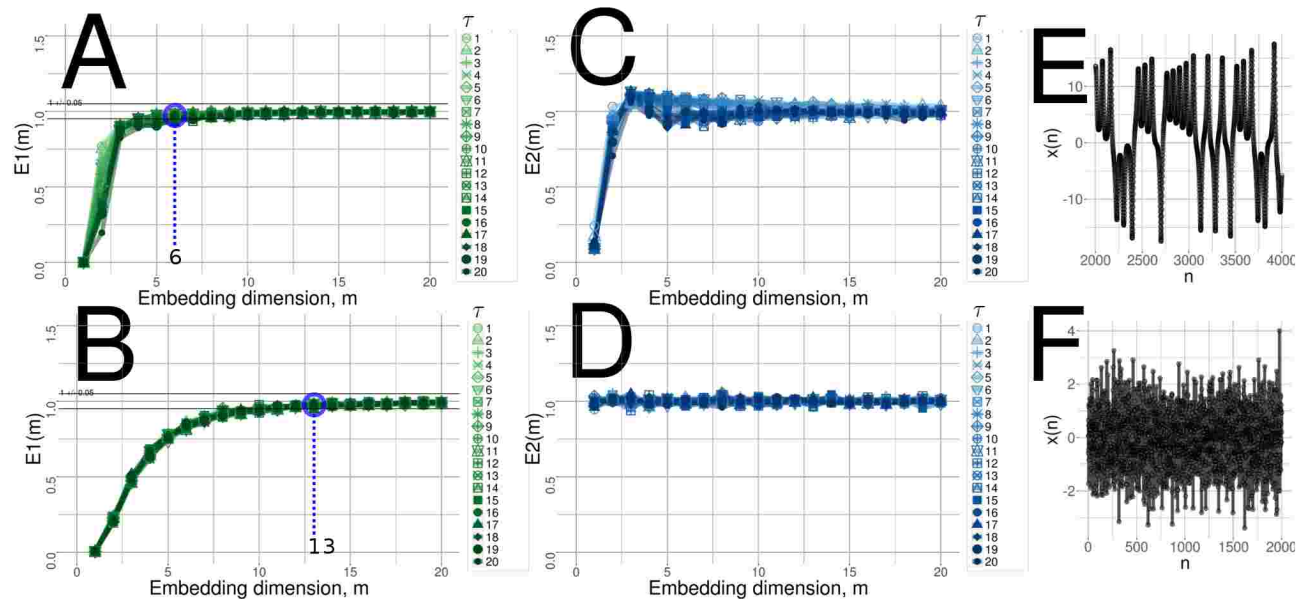


Figure 12. Minimum dimension embedding values with Cao’s method. (A, B) $E_1(m)$ values and (C, D) $E_2(m)$ values with variations of τ values from one to twenty for (E) chaotic and (F) random time series. Code and data to reproduce the figure is available in¹⁵.

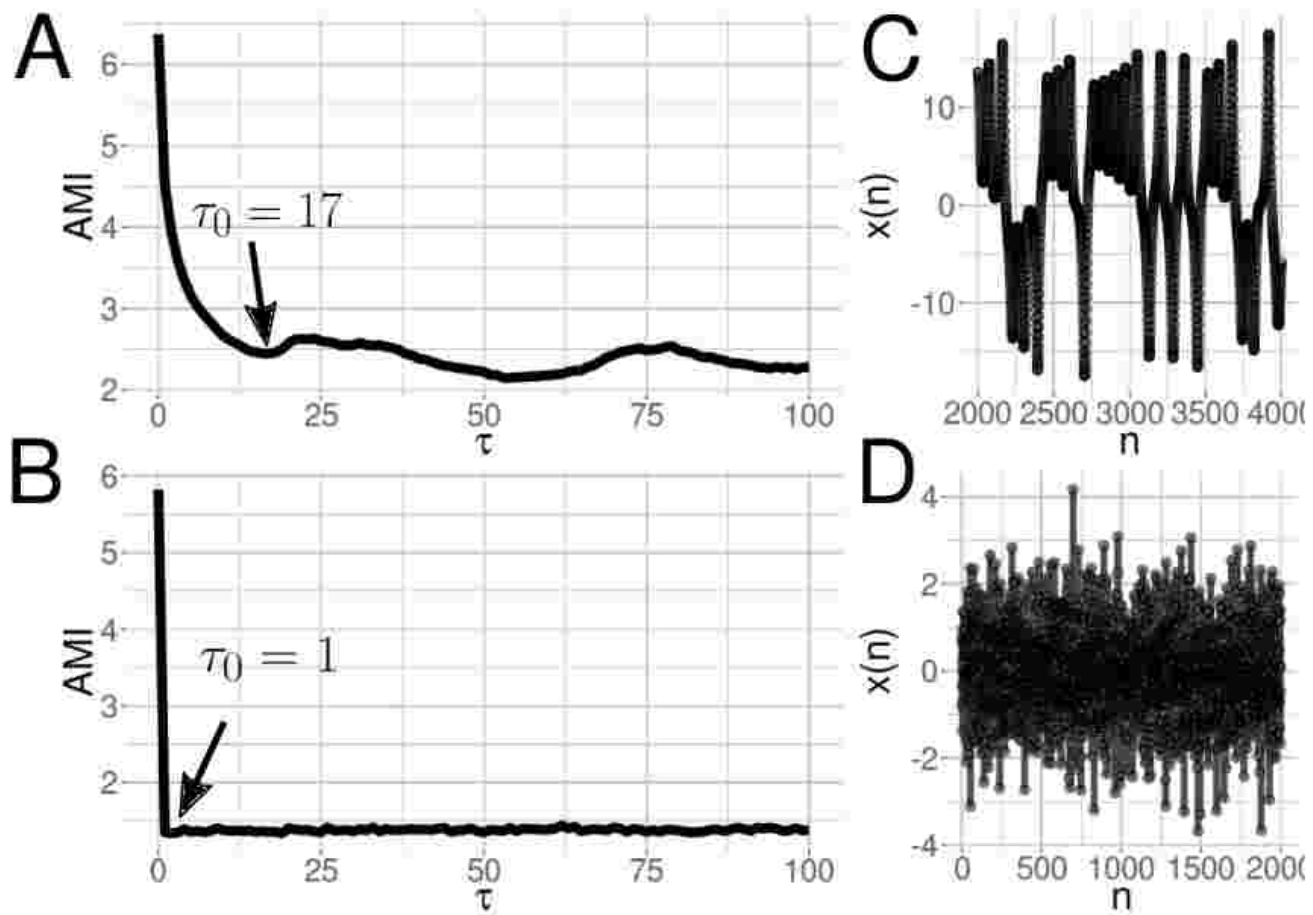


Figure 13. Minimum delay embedding values with AMI's method. (A, B) AMI values where its first minimum value in the curve is the minimum time delay embedding (τ_0), for (C) a chaotic and (D) noise time series. Code and data to reproduce the figure is available in¹⁵.

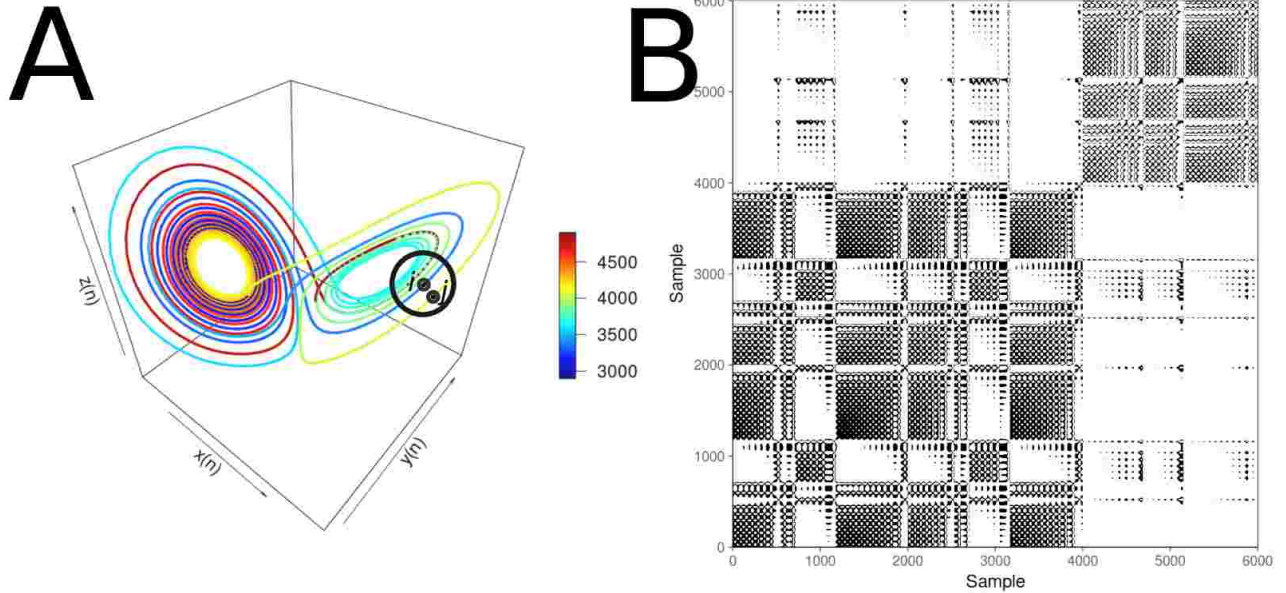


Figure 14. Recurrence Plots. (A) State space of the Lorenz system with controlling parameters ($\rho = 28, \sigma = 10, \beta = 8/3$). A point, j , in trajectory $X()$ which falls into the neighborhood (black circle) of a given point at i is a recurrent point and is represented as a black dot in the recurrence plot at location (i, j) or white otherwise. (B) Recurrence plot using the three components of the Lorenz system and the RP with no embeddings and threshold $\varepsilon = 5$. This figure is adapted from³⁴. Code and data to reproduce the figure is available in¹⁵.

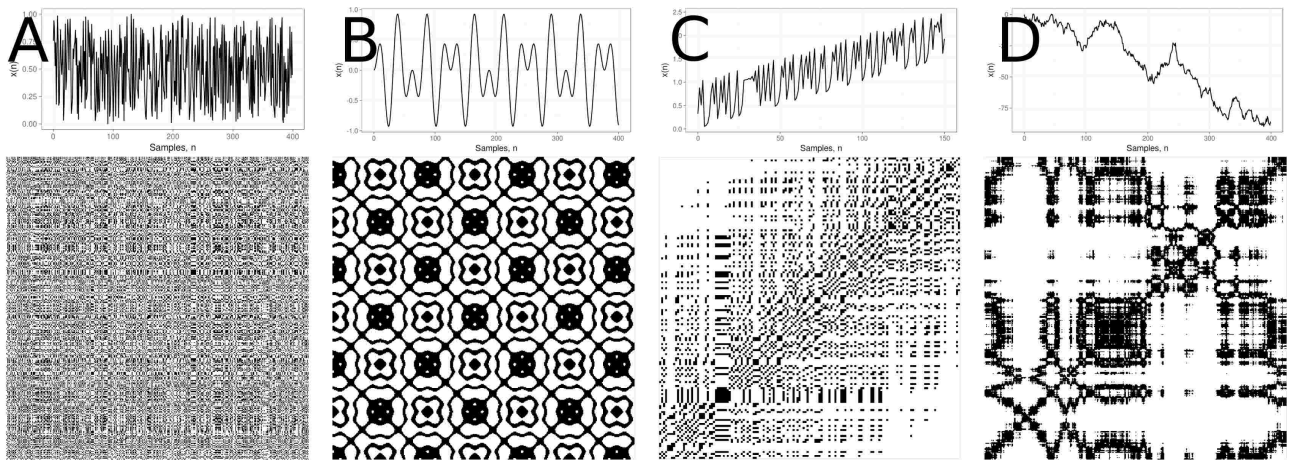


Figure 15. Patterns in Recurrence Plots. Time-series with its respective recurrence plot for: (A) uniformly distributed noise, (B) super-positionet harmonic oscillation ($\sin(\frac{1}{5} * t) * \sin(\frac{5}{100} * t)$), (C) drift logistic map ($x_{i+1} = 4x_i(1 - x_i)$) corrupted with a linearly increase term ($0.01 * i$), and (D) disrupted brownian motion ($x_{i+1} = x_i + 2 * rnorm(1)$). This figure is adapted from³⁴. Code and data to reproduce the figure is available in¹⁵.

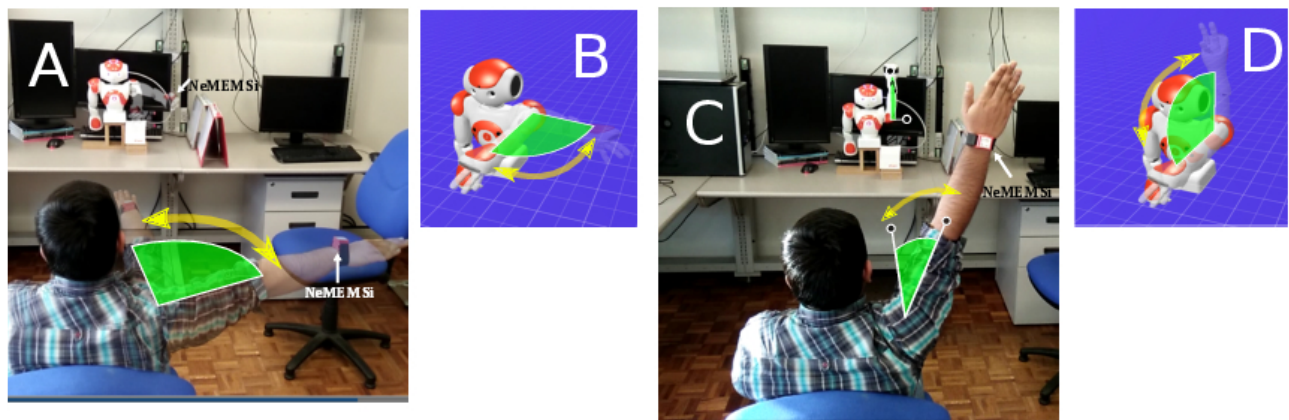


Figure 16. Human-humanoid imitation activities. Face-to-face human-humanoid imitation (HHI) activities for (A) HHI of horizontal arm movement, (B) Humanoid horizontal arm movement, (C) HHI of vertical arm movement, and (D) Humanoid vertical arm movement.

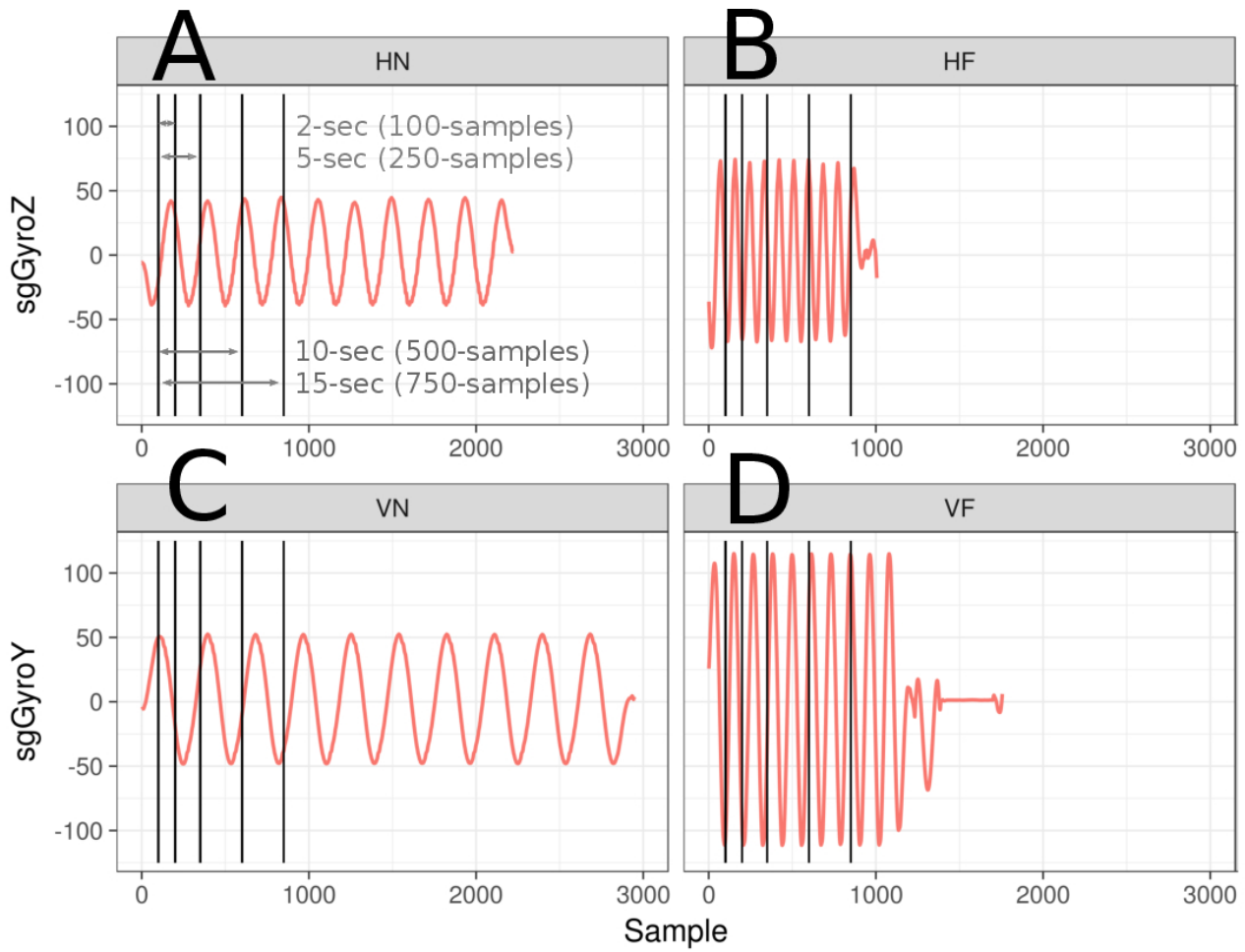


Figure 17. Time series duration of horizontal and vertical arm movements. Time series of smoothed data from gyroscope sensor for different speed arm movements performed by NAO: (A) Horizontal Normal arm movement (HN), (B) Horizontal Faster arm movement (HF), (C) Vertical Normal arm movement (VN) and (D) Vertical Faster arm movement (VF). Additionally, (A) shows window sizes for 2-seconds (100 samples), 5-seconds (250 samples), 10-seconds (500 samples) and 15-seconds (750 samples) which are also presented in (B), (C) and (D). Code and data to reproduce the figure is available in [15](#).

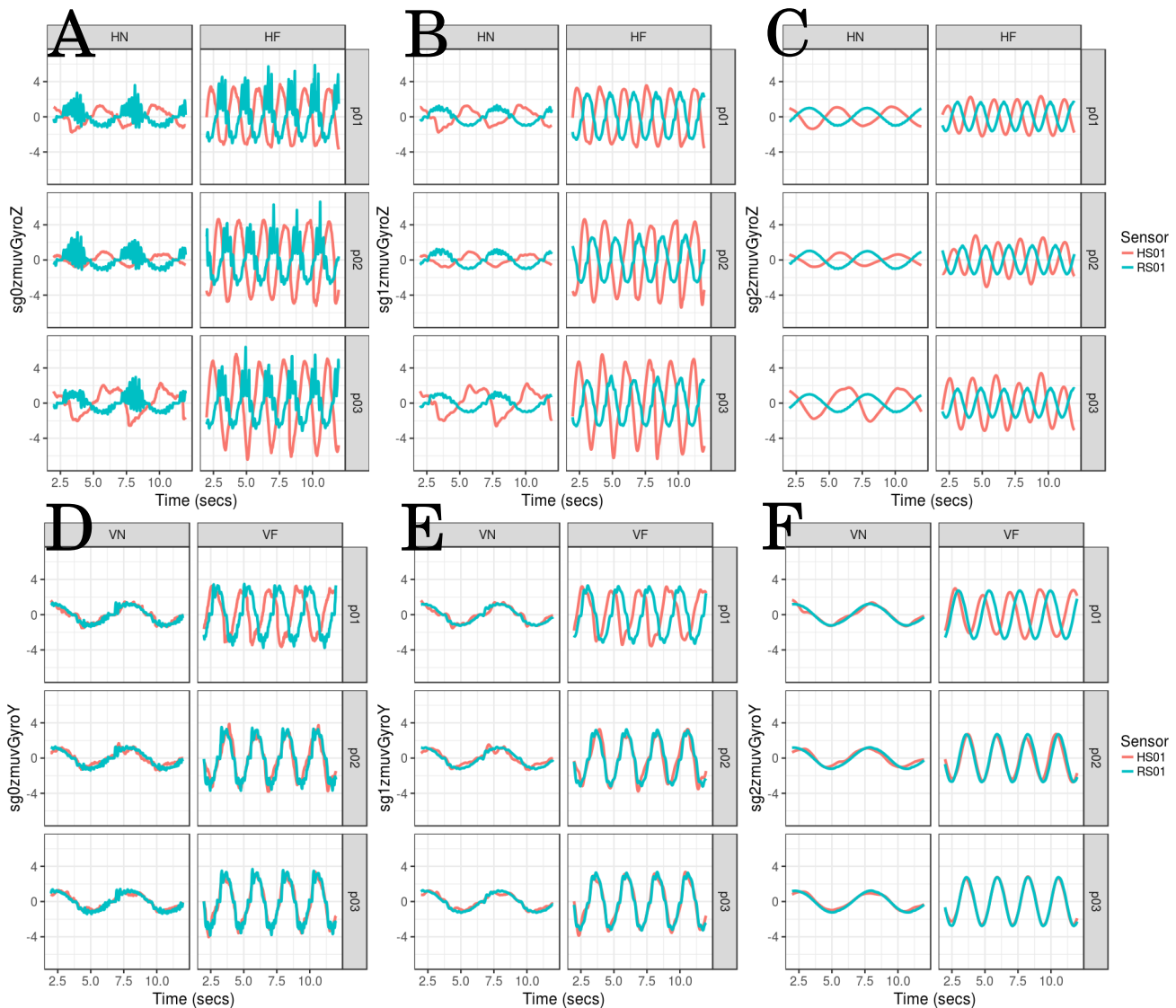


Figure 18. Time series for horizontal and vertical arm movements. (A/D) raw-normalised (sg0zmuv), (B/E) normalised-smoothed 1 (sg1zmuv) and (C/F) normalised-smoothed 2 (sg2zmuv). Time series are only for three participants ($p01$, $p02$, and $p03$) for horizontal and vertical arm movements in normal and faster velocity (HN, HF, VN, VF) with the normalised GyroZ or GyroY axis and with one sensor attached to the participant (HS01) and other sensor attached to the robot (RS01). Code and data to reproduce the figure is available in¹⁵.